REVIEWS OF MODERN PHYSICS, VOLUME 92, OCTOBER–DECEMBER 2020

Colloquium: Unusual dynamics of convection in the Sun

Jörg Schumacher[*]

Institut für Thermo- und Fluiddynamik, Technische Universität Ilmenau,
D-98684 Ilmenau, Germany
and Tandon School of Engineering, New York University, New York, New York 11201, USA

Katepalli R. Sreenivasan[†]

Tandon School of Engineering, New York University, New York, New York 11201, USA,
Department of Physics and Courant Institute of Mathematical Sciences,
New York University, New York, New York 10012, USA,
and Center for Space Science, New York University Abu Dhabi,
Abu Dhabi 129188, United Arab Emirates

(published 7 October 2020)

The Sun is our nearest star; it is also the most important star that determines life on Earth. A large variety of phenomena observed on the Sun's surface, with potential impact on Earth, is thought to arise from turbulent convection in Sun's interior, this being the dominant mode of heat transport within the outer envelope at $r \gtrsim 0.715 R_\odot$. However, convection in the Sun differs in most of its aspects from convection processes known on Earth, certainly those under controlled laboratory conditions, thus seriously challenging existing physical models of convective turbulence and boundary conditions in the Sun. Solar convection is a multiscale-multiphysics phenomenon including the transport of mass, momentum, and heat in the presence of rotation, dynamo action, radiation fluxes, and partial changes in chemical composition. Standard variables of state such as pressure, mass density, and temperature vary over several orders of magnitude within the convection region, thus introducing immense stratification. Although the Sun has been explored intensely, observational evidence on the structure and intensity of turbulent convection processes remains indirect and essentially limited to observations of the granular convection patterns at the surface and helioseismologic data that probe the propagation of sound waves in the interior. In this Colloquium characteristic scales and dimensionless parameters are discussed, particularly from the perspective of laboratory convection, a research field that has progressed significantly in the last few decades. The estimates and calculations of solar conditions given here are based mostly on the standard solar model S of Christensen-Dalsgaard *et al.*, which is a mean field model of solar convection. Light is shed on existing results to gain a deeper understanding of dynamical aspects of solar convection.

DOI: 10.1103/RevModPhys.92.041001

CONTENTS

I. INTRODUCTION

A central paradigm of solar physics today, which we comment upon toward the end of the Colloquium, is that all solar activity is driven by the internal dynamics alone

---

[*] joerg.schumacher@tu-ilmenau.de
[†] katepalli.sreenivasan@nyu.edu

0034-6861/2020/92(4)/041001(25)

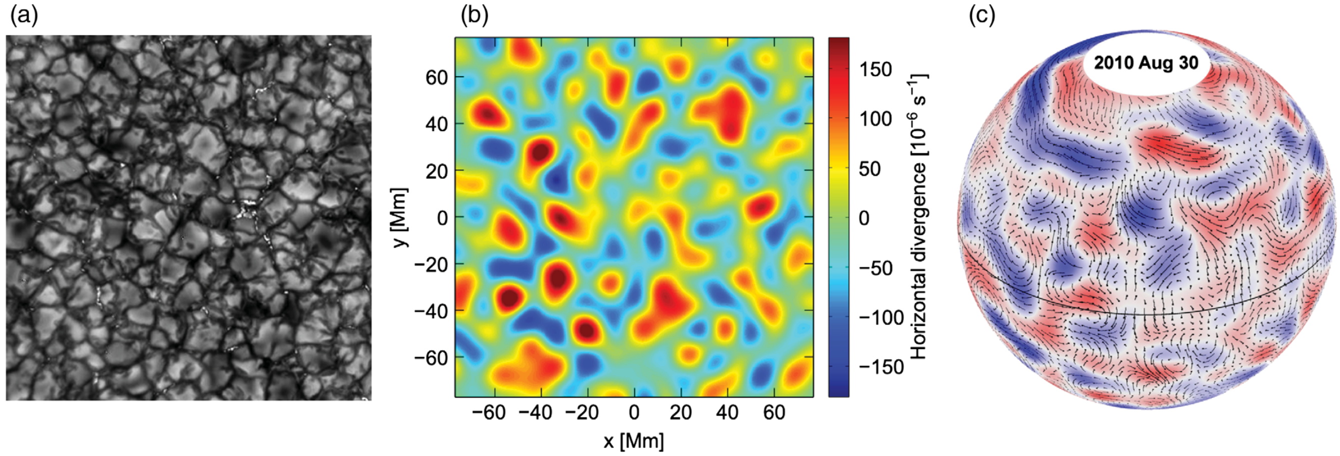

FIG. 1. Solar convection patterns at different scales. (a) Granulation. The characteristic length, time, and velocity scales of the granules are, respectively, $\ell_G \approx 1000$ km, $\tau_G \approx 10$ min, and $v_G \approx 3$ km/s. More details on granulation can be found, for example, in Abramenko *et al.* (2012) and Riethmüller *et al.* (2014). (b) Supergranulation indicated by horizontal surface flow divergences. The characteristic length, time, and velocity scales are, respectively, $\ell_{SG} \approx 3 \times 10^4$ km, $\tau_{SG} \approx 24$ h, and $v_{SG} \approx 500$ m/s; see also Rincon and Rieutord (2018). Langfellner, Gizon, and Birch (2015a) shared similar images. (c) Giant cells. The characteristic length, time, and velocity scales are estimated to be $\ell_{GC} \sim H \sim 2 \times 10^8$ m, $\tau_{GC} \approx 1$ month, and $v_{GC} \sim 10$ m/s, respectively (Hathaway, Upton, and Colegrove, 2013). Their interpretation is still in question.

(Christensen-Dalsgaard *et al.*, 1996; Miesch, 2005; Nordlund, Stein, and Asplund, 2009). In particular, internal convection is thought to affect the structure of the Sun and determine its appearance, especially with respect to the details occurring at the surface, such as granules and supergranules, the magnetic field generated by dynamo action, and its explosive events that impact weather and communication in space and on Earth. This puts a large onus on the need to better understand convection in the Sun. One challenge is to explain how the sea of stochastic activities characteristic of high-Reynolds-number turbulence due to convection coexists with recurrent phenomena such as sunspots, the regular alternation of their polarities with each cycle, the decrease in latitude of the activity as the cycle progresses, its approximate symmetry about the equator, etc. This challenge is compounded by the limitations of the tools available to study solar convection: Controlled laboratory measurements are not directly relevant to conditions in the Sun, direct observations are possible only on the surface, and we cannot solve the equations completely, either theoretically or computationally. Fortunately, helioseismology informs us, albeit indirectly, about some aspects of the interior structure (Christensen-Dalsgaard, 2002; Hanasoge, Gizon, and Sreenivasan, 2016); we know the basic equations from which to create models for both analytical and computational studies; and laboratory experiments provide various useful metaphors of physical understanding; see, e.g., Siggia (1994), Kadanoff (2001), Ahlers, Grossmann, and Lohse (2009), and Chillà and Schumacher (2012).

Convection in the Sun is known to start outward of $r_* \approx 0.715 R_\odot$, where $R_\odot = 6.96 \times 10^8$ m is the radius of the Sun (Kippenhahn, Weigert, and Weiss, 2012), under combinations of extreme conditions: (1) the fluid medium is a complex and highly stratified plasma; (2) Rayleigh and Reynolds numbers (both hydrodynamical and magnetic) are extremely large, indeed, much larger than those encountered terrestrially, thus leading to the expectation of a strongly turbulent convective flow; (3) radiative transport; (4) extremely small molecular Prandtl numbers, discussed already by Ledoux, Schwarzschild, and Spiegel (1961), particularly for the temperature, create new conceptual and computational challenges; and (5) rotation effects are important directly at the largest scales and indirectly on smaller ones. As examples, the temperature across the convection zone (CZ) drops from $T \approx 2 \times 10^6$ K at the bottom (Christensen-Dalsgaard *et al.*, 1996) to $T \approx 5779$ K at the surface (Böhm-Vitense, 1954); the mass density varies over more than 6 orders of magnitude and the flow speeds reach from subsonic in most of the CZ to locally supersonic on the surface; the pressure of the plasma at the bottom of the convection zone, corresponding to a value of $p \approx 6 \times 10^{12}$ Pa, is roughly equivalent to a mass of 10^7 tons acting on a square meter with an acceleration due to gravity g of about 600 m/s^2. The scale heights of density, pressure, and temperature vary over several orders of magnitude within the CZ and become, toward the surface, by a factor of 1000 smaller than the total height of the CZ, which is $H \approx 2 \times 10^8$ m.

For a solar physicist with an interest in computing and understanding the turbulent dynamics in the Sun, it is still difficult to ascertain with confidence some of the appropriate conditions and parameters. These estimates are particularly essential for inquiring how convection in the Sun can support a wide range of loosely organized scales illustrated in Fig. 1. One purpose of this Colloquium is to provide the best information possible at the level of our current understanding; we know of no place where this information can be found readily. Further, we might inquire into the extent to which recent work on turbulent convection can teach us about solar convection beyond the mixing length theory and related developments. In particular, we shed light on the radial variations of the Rayleigh and Prandtl numbers (both thermal and magnetic) and their connection to typical scales, velocities, and times. Emphasis is given to the case of extremely small Prandtl numbers and its likely implications for existing solar convection models. We also discuss some implications of our findings on the dynamical effects, including rotation and magnetic fields. Given space restrictions, parts of this discussion is limited to basic aspects.

From the fluid mechanics perspective, the most general set of equations considers compressible magnetoconvection with radiation and rotation (which is moderate and differential in character). It is useful to present them here even though all existing numerical or analytical models solve only simplified versions of these complete forms. The equations comprise the balance equations of the mass density ρ given by Eq. (1), the momentum density $\rho\boldsymbol{u}$ given by Eq. (2) with velocity field $\boldsymbol{u}$, the energy density $\rho e = \rho h - p$ (with enthalpy density ρh and pressure p) given by Eq. (3), and the magnetic induction $\boldsymbol{B}$ given by Eq. (4) (Tritton, 1988; Ossendrijver, 2003; Brandenburg and Nordlund, 2011; Weiss and Proctor, 2014):

$$\frac{D\rho}{Dt} = -\rho(\nabla\cdot\boldsymbol{u}), \tag{1}$$

$$\rho\frac{D\boldsymbol{u}}{Dt} + 2\rho(\boldsymbol{\Omega}\times\boldsymbol{u}) = -\nabla p + \boldsymbol{j}\times\boldsymbol{B} + \nabla\cdot\hat{\boldsymbol{\sigma}} + \rho\boldsymbol{g}, \tag{2}$$

$$c_p\rho\frac{DT}{Dt} - \frac{Dp}{Dt} = \nabla\cdot(k\nabla T) + 2\eta\hat{\boldsymbol{\Sigma}}:\hat{\boldsymbol{\Sigma}} + \frac{j^2}{\sigma} + Q_{\rm rad}, \tag{3}$$

$$\frac{D}{Dt}\left(\frac{\boldsymbol{B}}{\rho}\right) = \frac{\boldsymbol{B}}{\rho}\cdot\nabla\boldsymbol{u} - \frac{1}{\rho}\nabla\times\left(\frac{\boldsymbol{j}}{\sigma}\right), \tag{4}$$

$$\nabla\cdot\boldsymbol{B} = 0, \tag{5}$$

$$\boldsymbol{j} = \frac{1}{\mu_0}\nabla\times\boldsymbol{B}. \tag{6}$$

The equations are closed with an equation of state for a mixture of N_s different species given by

$$p = (n_e + n_a)k_B T = \left(\sum_{k=1}^{N_s} x_k\psi_k + 1\right)\mathcal{R}\rho T, \tag{7}$$

where $\mathcal{R} = k_B/m_u\bar{\mu}$ is the specific gas constant with the mean molecular weight $\bar{\mu}$, n_e is the electron number density, $x_k = n_{i,k}/n_k$ is the first ionization degree of element k, n_k is the number density of neutral atoms of element k, and $\psi_k = n_k/\sum_k n_k = n_k/n_a$ is the relative abundance (Vögler *et al.*, 2005). Here k_B is the Boltzmann constant, μ_0 is the permeability of free space, and m_u is the atomic mass unit. The quantity $\boldsymbol{\Omega}$ is the angular frequency, $\boldsymbol{g}$ is the acceleration due to gravity, and $\hat{\boldsymbol{\sigma}}$ is the compressible viscous stress tensor field

$$\hat{\boldsymbol{\sigma}} = 2\eta\hat{\boldsymbol{S}} + \left(\zeta - \frac{2}{3}\eta\right)(\nabla\cdot\boldsymbol{u})\hat{\boldsymbol{I}}, \tag{8}$$

with the dynamic (shear) viscosity η, the rate-of-strain tensor $\hat{\boldsymbol{S}} = (\nabla\boldsymbol{u} + \nabla\boldsymbol{u}^T)/2$, and the Kronecker tensor $\hat{\boldsymbol{I}}$. For the bulk viscosity $\zeta = 0$ Eq. (8) can be written as $\hat{\boldsymbol{\sigma}} = 2\eta\hat{\boldsymbol{\Sigma}}$; this term enters viscous dissipation in the energy balance (3). Equations (5) and (6) comprise, respectively, the divergence constraint of the magnetic induction field $\boldsymbol{B}$ and the Ampère law for the current density $\boldsymbol{j}$. Besides η, further (space-dependent) material parameters in Eqs. (1)–(6) are the electrical conductivity σ, the thermal conductivity k, and the specific heat at constant pressure c_p. Kinematic viscosity is given by $\nu = \eta/\rho$ and temperature diffusivity is given by $\kappa = k/\rho c_p$. See the Supplemental Material (245) for other physical constants such as k_B or m_u.

The energy balance (3) contains a source field due to local radiative cooling and heating $Q_{\rm rad}(\boldsymbol{x})$, which is given as an integral over the electromagnetic spectrum in combination with an average over the solid angle Ω:

$$Q_{\rm rad} = 4\pi\rho\int_\lambda \mathcal{K}_\lambda\left(\frac{1}{4\pi}\int_\Omega [I_\lambda(\boldsymbol{n}) - S_\lambda(\boldsymbol{n})]d\Omega\right)d\lambda. \tag{9}$$

Here $\mathcal{K}_\lambda(\boldsymbol{x})$ is the monochromatic opacity field of the plasma at wavelength λ, $I_\lambda(\boldsymbol{x},\boldsymbol{n})$ is the monochromatic intensity, and $S_\lambda(\boldsymbol{x},\boldsymbol{n})$ is the monchromatic source field. The monochromatic intensity I_λ is determined by the static radiative transport equation ($\boldsymbol{n}$ is the beam direction)

$$\boldsymbol{n}\cdot\nabla I_\lambda(\boldsymbol{x},\boldsymbol{n}) = \rho(\boldsymbol{x})\mathcal{K}_\lambda(\boldsymbol{x})[S_\lambda(\boldsymbol{x},\boldsymbol{n}) - I_\lambda(\boldsymbol{x},\boldsymbol{n})]. \tag{10}$$

The opacity is determined by the local plasma conditions and thus by the equation of state. This feature implies the assumption of a local thermodynamic equilibrium as discussed by Chandrasekhar (1960). With increasing depth the two terms on the right-hand side of Eq. (10) approach each other, and radiation can be treated by diffusion approximation for an optically thick medium, as $Q_{\rm rad}(r) \approx \partial_r[k_{\rm rad}(r)\partial_r T]$ (Nordlund, Stein, and Asplund, 2009). Typically shorter intervals of the spectrum are collected into bins and Eq. (10) is solved by ray-tracing methods; see the Supplemental Material (245) for more details.

Five essential dimensionless parameters can be extracted from the set of equations: the Rayleigh number Ra, thermal and magnetic Prandtl numbers Pr and Pm, the Rossby number Ro, and the Chandrasekhar number Q. These parameters are given by

$$\mathrm{Ra} = \frac{g_r\varepsilon_r H_r^3}{\nu_r\kappa_r}, \tag{11}$$

$$\mathrm{Pr} = \frac{\nu_r}{\kappa_r}, \tag{12}$$

$$\mathrm{Pm} = \mu_0\sigma_r\nu_r, \tag{13}$$

$$\mathrm{Ro} = \frac{U_r}{2H_r\Omega_r}, \tag{14}$$

$$Q = \frac{\sigma_r B_r^2 H_r^2}{\rho_r\nu_r}. \tag{15}$$

Of these, Pr and Pm are characteristic of the fluid and the rest are combinations of fluid and flow properties; all are strongly dependent on the radial position in the CZ. The subscript r here indicates a reference value such that local (or scale-resolved) definitions of the parameters are also possible.

TABLE I. Characteristic scales and dimensionless parameters of the Sun in comparison to selected terrestrial experiments in Rayleigh-Bénard convection (RBC) and rotating Rayleigh-Bénard convection (rRBC). Here r_*, $R_\odot$, and r_g are the radius at the bottom of the convection zone, the solar radius, and the geometric mean of the two, respectively. Scale estimates for the Sun are based on model S. The estimates for the experiments have been collected from Niemela *et al.* (2000) for RBC in He, from Glazier *et al.* (1999) for RBC in Hg, and from Ecke and Niemela (2014) for rRBC in He; they were selected because they reached the highest Ra in each category. The same high Rayleigh number as in rRBC was obtained in RBC by Weiss, Wei, and Ahlers (2016) in a cylindrical cell of aspect ratio 1 with a height of $H = 24.8$ cm using the fluorocarbon 3M Fluorinert FC72 at $\mathrm{Pr} = 12.3$ and $\mathrm{Ro} \geq 0.1$. The pressure scale height in Boussinesq and near-Boussinesq experiments is extremely large compared to the height of the cell. Ra, Ro, Q, and Re for the Sun are based on the free-fall velocity U_f and the pressure scale height $\mathcal{H}_p$. We used $\eta_\mathrm{K} = \mathcal{H}_p \mathrm{Re}_f^{-3/4}$, $\eta_\mathrm{OC} = \eta_\mathrm{K}\,\mathrm{Pr}^{-3/4}$, and $\eta_\mathrm{J} = \eta_\mathrm{K}\mathrm{Pm}^{-3/4}$.

		Solar CZ		RBC in He	RBC in Hg	rRBC in He
	$r = r_*$	$r = r_g$	$r = R_\odot$			
Layer height H		1.98×10^8 m		1 m	0.6 m	1 m
Kolmogorov scale η_K	60 mm	5.3 mm	3.2 mm	6 mm–1 μm	2 mm–11 μm	0.3 mm–50 μm
Obuhkov-Corrsin scale η_OC	1.9 km	0.17 km	18000 km	8 mm–0.08 μm	32 mm–170 μm	0.4 mm–65 μm
Joule dissipation scale η_J	1.9 m	0.9 m	18 m	$\cdots$	$\cdots$	$\cdots$
Pressure scale height $\mathcal{H}_p$	6×10^7 m	3×10^7 m	10^5 m	∞	∞	∞
Rayleigh number Ra	10^{18}	10^{20}	10^{12}	10^6–10^{17}	10^5–10^{11}	4×10^9–4×10^{11}
Thermal Prandtl number Pr	10^{-6}	10^{-6}	10^{-13}	0.7–30	0.025	0.7
Magnetic Prandtl number Pm	10^{-2}	10^{-3}	10^{-5}	$\cdots$	$\cdots$	$\cdots$
Rossby number Ro	1	10	10^5	$\cdots$	$\cdots$	0.05–7
Chandrasekhar number Q	3×10^{20}	2×10^{20}	10^{18}	$\cdots$	$\cdots$	$\cdots$
Reynolds number Re	10^{12}	10^{13}	10^{10}	10^3–10^8	2×10^3–2×10^6	6×10^4–6×10^5

The Rayleigh number Ra contains the dimensionless superadiabaticity ε_r, which in standard Rayleigh-Bénard convection (RBC) is substituted by $\varepsilon_r \to \alpha\Delta T$ with the isobaric expansion coefficient α and the imposed temperature difference ΔT. This modification, which is discussed in more detail in Secs. IV.A and IV.B, stands for the temperature excess over the adiabatic equilibrium value and not the actual temperature excess (of about 2×10^6 K). The characteristic velocity U_f, which corresponds to a free-fall velocity in RBC, is given by

$$U_f = \sqrt{g_r \varepsilon_r H_r}, \tag{16}$$

from which the fluid and magnetic Reynolds (Rm) numbers follow as

$$\mathrm{Re}_f = \frac{U_f H_r}{\nu_r} = \sqrt{\frac{\mathrm{Ra}}{\mathrm{Pr}}} = \sqrt{\mathrm{Gr}}, \tag{17}$$

$$\mathrm{Rm}_f = \mu_0 \sigma_r U_f H_r = \frac{\mathrm{Re}_f}{\mathrm{Pm}}, \tag{18}$$

with Gr a Grashof number.

A representative estimate of the Rayleigh number, computed at the geometric mean radius $r_g = \sqrt{r_* R_\odot} = 0.845 R_\odot$ and $\Delta T \approx 6000$ K, which is the approximate superadiabatic excess temperature (see Sec. IV.A for details), yields $\mathrm{Ra} \sim 10^{23}$, which is at least 6 orders of magnitude larger than the largest result obtained to date in laboratory experiments of helium at $\mathrm{Ra} \leq 10^{17}$ and $\mathrm{Pr} \gtrsim 1$ (Niemela *et al.*, 2000), and 8 orders of magnitude larger than the sulfur hexafluoride experiments with $\mathrm{Ra} \leq 2 \times 10^{15}$ and $\mathrm{Pr} = 0.8$ (Ahlers *et al.*, 2012), both in cylindrical cells of aspect ratio (diameter to height) of $1/2$. The largest Rayleigh number attained computationally is 10^{15} for an aspect ratio of 0.1 and $\mathrm{Pr} = 1$; see Iyer *et al.* (2020). It has also been well known since the time of the pioneering work of Spiegel (1962) that turbulent convection in stellar interiors occurs at extremely low Prandtl numbers, which are smaller by at least 3 orders of magnitude than anything that can be obtained in laboratory experiments on Earth. The lowest Pr value reported in experiments for cells with aspect ratios $\Gamma \gtrsim 1$ is for liquid sodium with $\mathrm{Pr} = 0.005$ to 0.006 (Cioni *et al.*, 1997; Horanyi, Krebs, and Müller, 1999) at Rayleigh numbers $\mathrm{Ra} \sim 10^6$; for thermal convection in mercury at $\mathrm{Pr} = 0.021$, Rayleigh numbers $\mathrm{Ra} \lesssim 10^{11}$ were reported by Glazier *et al.* (1999). Direct numerical simulations of the convection equations, carried out via pseudospectral and spectral element techniques, have reached $\mathrm{Pr} = 0.01$ at $\mathrm{Ra} = 5 \times 10^6$ (Petschel *et al.*, 2013) and $\mathrm{Pr} = 0.005$ at $\mathrm{Ra} = 10^7$ (Schumacher *et al.*, 2016; Scheel and Schumacher, 2017). Thus, solar convection lies in parameter ranges outside our terrestrial experience (including laboratory experiments and numerical simulations). Table I compares some characteristic scales and dimensionless parameters in solar convection with those of terrestrial studies.

Part of our present understanding of the velocity of the fluid in the solar convection zone is based on standard algebraic turbulence models such as the mixing length model by Vitense (1953), Böhm-Vitense (1958), and Spruit (1974); unfortunately, it is not clear that mixing length models are applicable to the Sun (or to any multiscale turbulent flow). We have also learned from large-scale simulations of the equations of motion, e.g., Miesch *et al.* (2012) and Hindman, Featherstone, and Julien (2020), that the Rayleigh numbers attained in the simulations are much smaller than that characteristic of the Sun. Observational data from helioseismology, which are based on acoustic modes that are excited by near-surface convective turbulence with characteristic velocities at the speed of sound (Spruit, Nordlund, and Title, 1990; Christensen-Dalsgaard, 2002; Gizon, Duvall, and Schou, 2003; Hanasoge, Gizon, and Sreenivasan, 2016), have also provided valuable information. The amplitudes of these

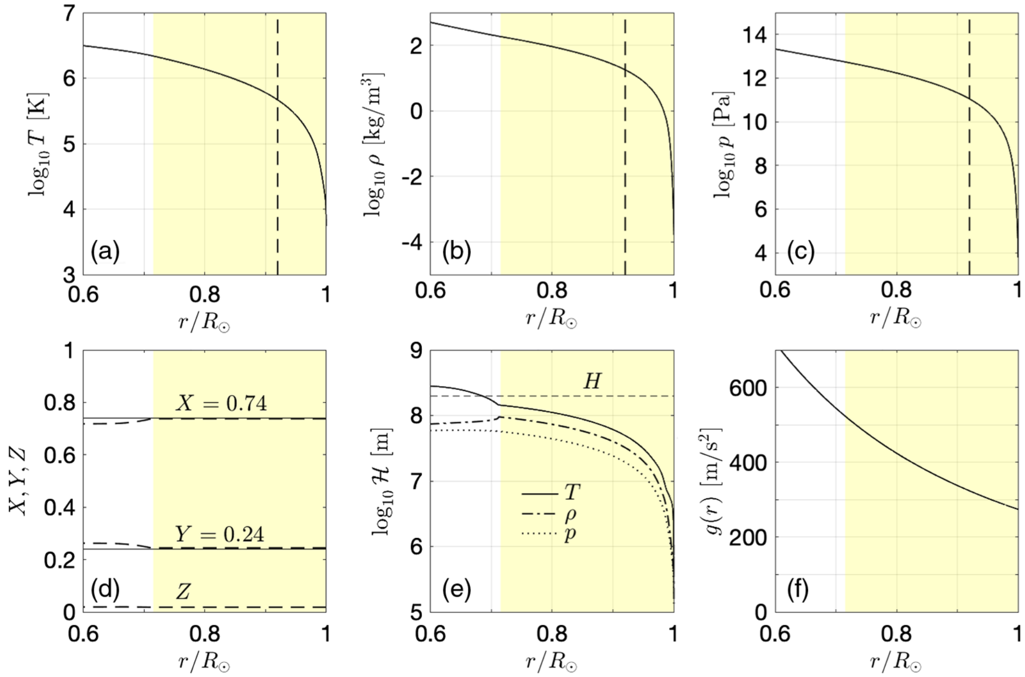

FIG. 2. Radial dependence of (a) temperature T, (b) mass density ρ, and (c) pressure p across the CZ from model S. The temperature drops down to 5779 K at the solar surface. The vertical dashed lines indicate the depth to which helioseismology can access fluctuations in velocity. (d) Generally accepted abundances of hydrogen (X), helium (Y), and all heavier elements (Z). The thin solid lines indicate the typical values of $X = 0.74$ and $Y = 0.24$ in the CZ. (e) Scale heights of temperature, pressure, and density $\mathcal{H}_T$, $\mathcal{H}_p$, and $\mathcal{H}_\rho$. (f) Plot of the acceleration due to gravity. We indicate the extent of the CZ in all six panels by a shaded background, which starts at $r_* \approx 0.715 R_\odot$.

modes (sorted by their angular wave number) reflect the dynamics and energy conversions in the uppermost part of the solar convection zone. An inference of the characteristic velocities deeper in the bulk of the CZ is obtained by complex inversion tools, local helioseismology, and mode coupling analysis that reach roughly to a depth of $0.92 R_\odot$. In the region where data are available from multiple sources (Hanasoge, Gizon, and Sreenivasan, 2016; Nagashima *et al.*, 2020), the turbulent amplitudes are found to be much smaller than those predicted by convection models or alternative analysis methods (Greer *et al.*, 2015; Woodward, 2016); this conundrum has not yet been resolved satisfactorily, though steady progress is being made (Birch *et al.*, 2018).

II. STANDARD SOLAR MODEL

A. State variables and chemical composition

The reference state for the Sun (as for other stars) makes the following assumptions (Kippenhahn, Weigert, and Weiss, 2012): (i) spherical symmetry for all physical quantities due to self-gravity, (ii) a hydrostatic and isentropic equilibrium, and (iii) convection as a slight departure from equilibrium, described, at least to a working approximation, by the mixing length theory (Prandtl, 1925; Vitense, 1953; Böhm-Vitense, 1958; Spiegel, 1963). The slight overshoot layer at the bottom of the CZ, the tachocline, right above the stable radiation zone, is neglected. (iv) Local thermodynamic equilibrium exists for processes on scales $\langle\lambda\rangle \ll \ell \ll R_\odot$, where $\langle\lambda\rangle$ is the mean free path of electrons, ions, or photons; for this range of scales, material properties are homogeneous, the plasma is well mixed, and its state can be described by a set of macroscopic state variables that are functions of the radial coordinate r, the pressure $p(r)$, the temperature $T(r)$, and the mass density $\rho(r)$; see Sec. I. (v) Coupling to the magnetic fields can be neglected as far as dynamical behavior is concerned.

We specifically make use of the solar model S developed by Christensen-Dalsgaard *et al.* (1996). This model predicts self-consistently the radial profiles of all relevant physical quantities. They are summarized in Figs. 2(a)–2(c), which show that the state variables T, ρ, and p vary by several orders of magnitude across the CZ. This behavior implies that all typical scale heights, i.e., the heights over which the relevant quantity varies by an order of magnitude, are smaller than H, which is the largest scale in the problem (setting aside the solar radius itself). The scale heights of p, ρ, and T are defined as $\mathcal{H}_p = -dr/d\log p$, $\mathcal{H}_\rho = -dr/d\log\rho$, and $\mathcal{H}_T = -dr/d\log T$, respectively. For an ideal gas one gets $\mathcal{H}_p^{-1} = \mathcal{H}_\rho^{-1} + \mathcal{H}_T^{-1}$. Figure 2(e) shows their radial variations. Close to the surface, the pressure and density scale heights drop to values as small as $\mathcal{H}_p \sim \mathcal{H}_\rho \sim 10^2$ km, while the temperature scale height becomes $\mathcal{H}_T \sim 10^3$ km. This trend reflects the extremely strong stratification of all state variables close to the solar surface. Figure 2(d) provides the element abundances. Hydrogen (X) and helium (Y) dominate the plasma composition and appear at a fixed ratio across the entire CZ. Z denotes the remaining 2% of all heavier elements. These abundances, in particular, those of metals, are the subject of ongoing updates as discussed, for example, by Asplund *et al.* (2009); see also Sec. III.A. For the rest of this Colloquium, we keep the abundances as shown in Fig. 2(d); suitable changes will need to be made if these abundances get revised in the future.

The solar plasma is fully ionized for most of the CZ with respect to the lightest elements H and He since the temperatures are high enough that they correspond with zero number density of neutral atoms, with $n_a = 0$ in Eq. (7). Heavier elements retain some electrons only. Toward the solar surface, hydrogen and helium are only partly ionized. Thus, H, H_2, H^+ as well as He, He^+, and He^{2+} appear in a mixture that affects the thermodynamic properties such as the pressure or the specific heat at constant pressure and volume, $c_p(r)$ and $c_v(r)$. Helium is fully doubly ionized for $r \lesssim 0.92 R_\odot$. Hydrogen is fully ionized for $r \lesssim 0.98 R_\odot$, which corresponds to a plasma temperature $T \gtrsim 10^5$ K (Kippenhahn, Weigert, and Weiss, 2012).

Figure 2(f) plots the profile of the acceleration due to gravity, given by $g(r) = Gm(r)/r^2$, where $m(r)$, the solar mass up to a shell of radius r, and is defined as $m(r) = 4\pi \int_0^r \rho(r') r'^2 dr'$. All of these profiles suggest that transport quantities such as viscosity and thermal diffusivity are likely to vary with position along the radius; nor can one simply use the total height H or a fixed value of g in the definition of the Rayleigh number. It is thus clear that our discussion of flow parameters has to be refined.

B. The convection zone

Energy is generated by nuclear fusion converting about 6×10^8 tons of hydrogen to helium each second in the core of the Sun $r \lesssim 0.25 R_\odot$. The material in this region is hot ($\approx 1.57 \times 10^7$ K) and dense ($\approx 1.5 \times 10^5$ kg/m^3). Practically no fusion takes place beyond about $0.3 R_\odot$ and the energy in the region between the fusion region and $0.7 R_\odot$ is transported outward solely by radiation. The radiative flux is given by $F_r(r) = -k_\gamma dT/dr = L(r)/(4\pi r^2)$, where $L(r)$ is the solar luminosity at distance r from the center and k_γ is the thermal conductivity associated with photon transport; see Sec. III for more details. The radial temperature gradient that can transport the luminosity by outward radiation, thus sustaining the star in radiative equilibrium, is given by

$$\frac{dT}{dr} = -\frac{L(r)}{4\pi k_\gamma(r) r^2}. \tag{19}$$

The radial pressure profile is given by the hydrostatic equilibrium condition

$$\frac{dp}{dr} = -G\frac{m(r)\rho(r)}{r^2}, \tag{20}$$

where G is the universal gravitational constant. As already stated, we assume an ideal gas such that density, pressure, and temperature are related to each other by the equation of state; see Eq. (7). We define $\nabla := \partial \ln T / \partial \ln p$ and the combination of Eq. (19) and (20) results in

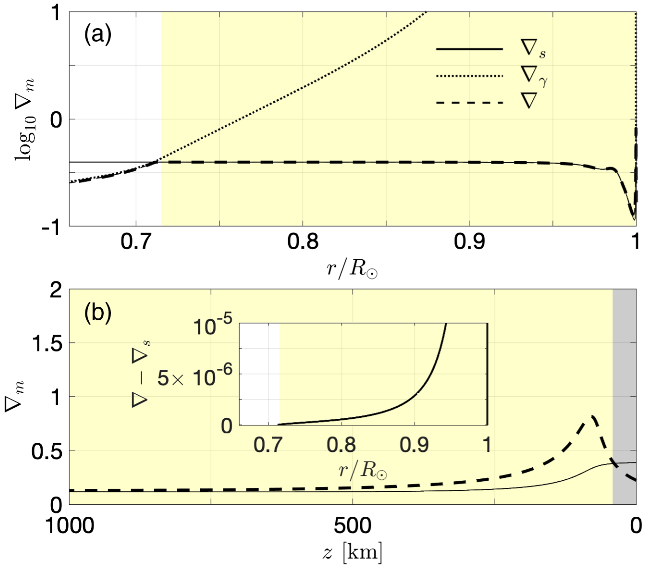

FIG. 3. Radial variation of the different dimensionless temperature derivatives ∇_m. Data are calculated from model S. (a) ∇_γ, ∇_s, and ∇ are shown across the entire convection zone (CZ), indicated as a shaded background. (b) Enlargement close to the solar surface. Depth z from the surface is given in km. The range where $\nabla_s > \nabla$ is darker shaded. Line styles are the same as in (a). (Inset) Superadiabaticity $\varepsilon = \nabla - \nabla_s$ across the CZ.

$$\nabla = \frac{L\mathcal{R}}{4\pi k_\gamma G m} =: \nabla_\gamma \tag{21}$$

in the radiation zone. Figure 3(a) confirms $\nabla(r) = \nabla_\gamma(r)$ for radii $r < r_* \approx 0.715 R_\odot$ using data of the standard solar model S. At a radius of $r = r_*$ the radiative transfer alone can no longer carry the fusion energy outward in a stable fashion. A second mechanism has to take over the transport, and it should be efficient even under a more gradual temperature gradient, and this is the thermal convection that generates the physical motion of the plasma, which transports the temperature effectively. A thin region of the solar interior just below the CZ, the so-called tachocline (Spiegel and Zahn, 1992), is somewhat unstable but we shall not discuss its dynamics in any detail. According to the Schwarzschild criterion [see Schwarzschild (1906) and Kippenhahn, Weigert, and Weiss (2012)], a layer becomes *unstable to convective motion*, or is superadiabatic, if

$$\frac{dT}{dr} < \left.\frac{dT}{dr}\right|_s = -\frac{g(r)}{c_p(r)} \quad \text{or} \quad \nabla_s(r) < \nabla(r), \tag{22}$$

where both radial temperature derivatives are negative. Adiabaticity is always indicated in the following by subscript s, which stands for constant specific entropy per unit mass. Quantities ∇_s, ∇_γ, and ∇, used in Eqs. (21) and (22), are the dimensionless adiabatic, radiative, and actual radial temperature derivatives, respectively. We recall that $\nabla_s = \gamma_{\rm ad}/(\gamma_{\rm ad} - 1) = 2/5$, and $\gamma_{\rm ad} = c_p/c_v = 5/3$ for a fully ionized ideal gas. Figure 3(a) shows that $\nabla_s = 2/5$ in the deep CZ and that ∇ exceeds the adiabatic exponent only slightly; ∇ almost coincides with ∇_s. The superadiabaticity $\varepsilon = \nabla - \nabla_s$

[see also Eq. (31) in Sec. IV.B] is plotted in the inset of Fig. 3(b). The difference of two gradients was approximated by the available data of model S to avoid the direct evaluation of ∇ by central finite differences with round-off errors. The superadiabaticity remains below 10^{-6} for the deep CZ and grows substantially only toward the outer solar surface, a region that is shown in detail in Fig. 3(b). This implies that the solar convection in most of the CZ is in a state that is extremely close to the marginal stability threshold with $\nabla_s \lesssim \nabla \ll \nabla_\gamma$ almost across the entire layer. Only for shallow depths smaller than 100 km from the average surface does one find $\nabla_s > \nabla$ [see the darker shaded region in Fig. 3(b)]; this is also true in the inner radiation zone for $r < r_*$. Convection near the surface is driven by the strong radiative outward cooling and $\nabla_\gamma < \nabla < \nabla_s$. It was discussed by Nordlund, Stein, and Asplund (2009) and Cossette and Rast (2016) that this extreme surface cooling due to radiation might be the major driver of turbulent convection in the entire CZ; the radiative flux that is released there is well known to be $L_\odot/(4\pi R_\odot^2) \approx 63\ \mathrm{MW/m^2}$.

C. The two layers of convection

The existence of a density scale height $\mathcal{H}_\rho$ that is far less than the convection layer thickness H suggests that the heavier material rising from the inside cannot be supported beyond a certain distance and has to reverse its direction; likewise, lighter and cooler material descending from the top layers of the Sun cannot penetrate completely below a certain radial distance. For this reason, it may be conceptually meaningful to think of convection in loosely connected multiple layers; indeed, the concept that turbulent thermal convection can be described as a sequence of ever thicker marginally unstable layers goes back to Malkus (1954). Nevertheless, it is both conventional and probably adequate for most purposes to think of only two layers of convection. The outer shallow layer, roughly 1% in radial thickness of the CZ, where the gradients are extreme and the temperatures are low enough for ionization to be only partial, sets itself apart from the rest of the CZ, where the gradients are smaller and the ionization is essentially complete. The power released by the Sun, which is of the order of 63 MW per square meter, results in extremely strong radiative cooling, which, as mentioned already, has been speculated to be the main driver of the turbulent convection processes in the Sun.

However, it is not obvious that this radiative cooling process drives the convection phenomena deep in the interior of the CZ ("deep" convection, which is all of the CZ except the outer layer). The horizontal scales of the surface granules are of the same order as the depth of the outer shallow layer convection $\ell \sim 10^3$ km; as this is a characteristic of convection in general, there is a suggestion here for the existence of a conceptually independent convection layer whose depth is of the same order of magnitude as the granular scales. While radiative cooling indeed drives convection in the outer shallow layer, the extreme gradients of density, temperature, and pressure near the surface could change the characteristics of the descending heavy fluid so strongly that one may imagine that the top shallow layer of convection does not have much to do *directly* with the rest of the CZ (except for providing the proper boundary condition). It might thus appear that one can study the surface layer and the bulk convection mechanisms as essentially distinct: for instance, Hotta, Iijima, and Kusano (2019) compare the results of massive simulations of the CZ, albeit without rotation and magnetic fields, performed with and without the solar surface layer, and find essentially no difference. However, descending dense vortex-ring-type thermals resulting from radiative cooling, known as entropy rain, may penetrate into the deep convection layer all the way to its bottom (Brandenburg, 2016; Anders, Lecoanet, and Brown, 2019). We discuss this point in Secs. IV and VI in more detail. Thus, while it is convenient to discuss the two zones somewhat separately, as we do in Sec. VI and in the Supplemental Material (245) when reviewing simulations, it must be stated that their coupling is a central problem of solar convection.

III. MOLECULAR TRANSPORT PARAMETERS

A. Radial dependence of transport coefficients

We calculate in this section the radial profiles of the three molecular diffusion coefficients and the resulting dimensionless parameters. Their extreme magnitudes are expected to generate a highly intermittent small-scale fluid turbulence, which in turn is affected by much coarser temperature and magnetic fields. This feature affects the modeling of unresolved scales. Most of the CZ comprises a collisional plasma that can be treated as an ideal, nonrelativistic, nondegenerate, and fully ionized gas that follows the rules of classical Maxwell-Boltzmann statistics (Reif, 2009). All three transport coefficients vary only in the radial direction as stipulated in the standard solar model S; the three transport coefficients are the dynamic viscosity η, thermal conductivity k, and electrical conductivity σ, which connect the linear response relations, respectively, of the viscous stress to the rate of strain in a Newtonian fluid $\hat{\boldsymbol{\sigma}} = 2\eta\hat{\boldsymbol{\Sigma}}$, of the heat flux to the temperature gradient, known as Fick's law $\boldsymbol{F} = -k\nabla T$, and of electrical current density to the electrical field, which is known as Ohm's law $\boldsymbol{j} = \sigma\boldsymbol{E}$. For simplicity, we assume isotropy of all transport processes and ignore the tensorial character of the three transport coefficients. In the Supplemental Material (245), we provide the detailed derivation of the temperature dependence of all transport coefficients. From there, one obtains the following transport coefficients (with temperature T in kelvin):

$$\sigma_e(r) \approx 8.2\times10^{-3}\,\frac{T^{3/2}(r)}{\bar{Z}_+^2\ln\Lambda_e(r)}\frac{1}{\Omega\,\mathrm{m}}, \tag{23}$$

$$\eta_i(r) \approx 5.1\times10^{-16}\,\frac{T^{5/2}(r)}{\bar{Z}_+^4\ln\Lambda_i(r)}\frac{\mathrm{kg}}{\mathrm{m\,s}}, \tag{24}$$

where the inverse of Eq. (23) is the well-known Spitzer resistivity (Spitzer, 1962). Here $\bar{Z}_+$ is the atomic number and the constants Λ_e and Λ_i are corrections due to the Debye shielding. The thermal conductivity is based on heat transfer by photons and given by

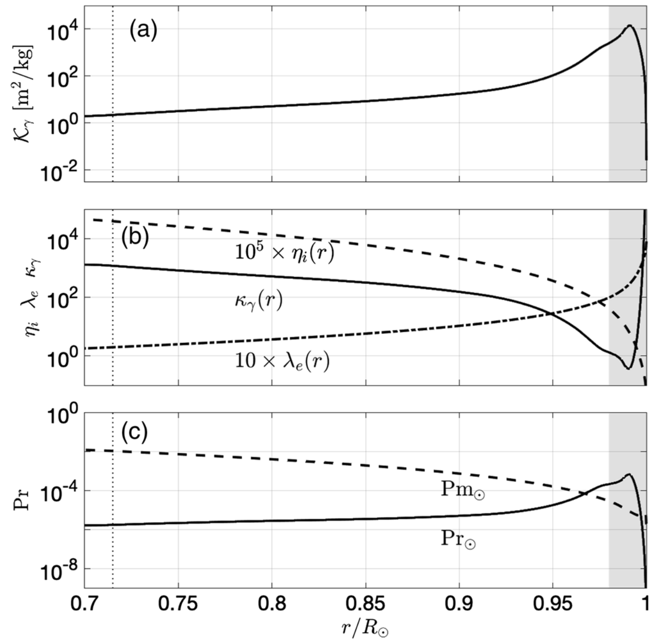

FIG. 4. (a) Opacity profile $\mathcal{K}_\gamma(r)$ in the solar convection zone. (b) Transport coefficients across the solar convection zone. The temperature diffusivity $\kappa_\gamma(r)$ in m^2/s, the dynamic viscosity $\eta_i(r)$ in kg/(m s), and the magnetic diffusivity $\lambda_e(r) = [\mu_0 \sigma_e(r)]^{-1}$ in m^2/s are shown. (c) Variation of the thermal and magnetic Prandtl numbers across the solar convection zone. The shaded area to the right stands for $r_i \gtrsim 0.98 R_\odot$, where the hydrogen of the solar plasma is partially ionized. The vertical dotted lines in all panels mark $r = r_*$.

$$k_\gamma(r) = \frac{16}{3} \frac{\sigma_B T^3(r)}{\mathcal{K}_\gamma(r)\rho(r)}. \tag{25}$$

This equation contains the coefficient $\mathcal{K}_\gamma$, the radiative cross section per unit mass, averaged over frequency, which is termed stellar opacity. The mean free path is now $\langle \lambda_\gamma \rangle = (\mathcal{K}_\gamma \rho)^{-1}$. Several processes can contribute to the scattering of photons and thus affect the stellar opacity (Kippenhahn, Weigert, and Weiss, 2012), for example, Thomson scattering, free-free absorption or inverse bremsstrahlung, bound-free absorption or photoionization, and bound-bound absorptions. These processes enter complex models for numerical opacity calculations at solar conditions, such as those of the Opacity Library project (Rogers and Iglesias, 1992, Iglesias and Rogers, 1996). Recent high-energy experiments that measure the opacity of heavier elements such as iron, chromium, and nickel (which are summarized as the solar metallicity) reveal discrepancies from former high-energy density plasma simulations (Nagayama *et al.*, 2019). As discussed by Basu (2019), different abundances of heavier elements could affect the number densities n_e at a given T and thus the position of the bottom of the CZ. Figure 4(a) displays the opacity $\mathcal{K}_\gamma$, which follows from the standard solar model S (Christensen-Dalsgaard *et al.*, 1996).

B. Thermal and magnetic Prandtl numbers

Figures 4(b) and 4(c) summarize the profiles of the transport coefficients and the resulting thermal and magnetic Prandtl numbers, which are given by

$$\mathrm{Pr}_\odot(r) = \frac{\nu_i}{\kappa_\gamma}, \qquad \mathrm{Pm}_\odot(r) = \mu_0 \sigma_e \nu_i. \tag{26}$$

The profiles for both Prandtl numbers are shown in Fig. 4(c). Both Prandtl numbers are extremely small, with a typical magnitude of $\mathrm{Pr}_\odot \sim 10^{-6}$ for the thermal case [see also Freytag *et al.* (2012)] and $\mathrm{Pm}_\odot \lesssim 10^{-2}$ in the magnetic case. Toward the surface of the Sun, the magnetic Prandtl number drops to about 10^{-5}, which is typical for liquid metal flow in laboratory; the thermal Prandtl number drops to extremely low values near the surface; and $\mathrm{Pr}_\odot \lesssim 10^{-13}$ in this calculation, but this will need to be revised as explained next. We mention here that Ledoux, Schwarzschild, and Spiegel (1961) had already estimated extremely small Prandtl numbers of the order of 10^{-9} within the framework of the Rayleigh-Bénard convection, which is discussed in Sec. VI.

The thermal Prandtl number $\mathrm{Pr}_\odot$ in the outer shell has to be corrected because the full ionization of the solar plasma cannot be maintained there. The permanent charge exchange and recombination processes (Bates, Kingston, and McWhirter, 1962; Fussen and Kubach, 1986) can be summarized by an effective recombination time τ_r that varies with depth. On the basis of a discussion by Landau and Lifshitz (1987), Cowley (1990) suggested that the bulk viscosity ζ can exceed the standard dynamic viscosity $\eta_i = \eta$ by orders of magnitude in the surface region; see Eq. (8). Landau and Lifshitz (1987) derived an expression for ζ for the case of quasiadiabatic time-periodic variations of a fluid property, such as the degree of ionization in the plasma denoted by x_k; see Eq. (7). These variations are driven by sound waves and result in $\zeta = \tau_r \rho (c_{s,\infty}^2 - c_s^2)/(1 - i\omega\tau)$, where τ_r is the effective relaxation (here recombination) time and ω is the typical angular frequency of the density variations; c_s is the speed of sound in the adiabatic case and $c_{s,\infty}$ is the speed of sound for frozen degrees of ionization. Since $\omega \tau_r \ll 1$, one gets

$$\zeta \simeq \rho \tau_r (c_{s,\infty}^2 - c_s^2) = \rho \tau_r \left(\frac{\partial p}{\partial \rho}\bigg|_{s,x} - \frac{\partial p}{\partial \rho}\bigg|_{s} \right). \tag{27}$$

Cowley (1990) presented calculations to a depth of 2000 km. The viscosity ratio ζ/η varied from $\zeta/\eta = 10^7$ at $r = R_\odot$ to $\zeta/\eta = 10^2$ at $z = 0.997 R_\odot$ (which corresponds with $z = 2000$ km). This causes an increase of the thermal Prandtl number to the same order of magnitude as that in the bulk of the convection zone. A more precise statement cannot be made at this point.

IV. DYNAMICAL ASPECTS OF THE CONVECTION ZONE

A. Mixing length theory

A successful model of convection requires a plausible energy transport mechanism. A dynamically acceptable description of convection has been elusive, but the mixing length theory (MLT) has been used to describe a variety of stellar observations, though it is regarded as conceptually implausible. The model was initiated by Prandtl in the aerodynamic context (Prandtl, 1925) and applied to the Sun by Vitense (1953) and Böhm-Vitense (1958); see also Chan and Sofia (1987), Spruit, Nordlund, and Title (1990), Barker, Dempsey, and Lithwick (2014), and Kupka and Muthsam (2017). According to this model, any transportable quantity is advected for a certain vertical distance, called the mixing length Λ, which is unknown *a priori*, without participating in any mixing; once the mixing length is traversed, however, the transportable quantity gives up its property to the new environment, and a perfect and instantaneous mixing takes place at this new position. All effects of turbulence enter the picture through a single scale, the mixing length Λ and the velocity V with which the transportable quantity is advected. The MLT picture is symmetric with respect to upward and downward motion, and one typically assumes that $\Lambda \propto \mathcal{H}_p$.

Refinements of MLT exist, such as the inclusion of the full energy spectrum of eddies by Canuto and Mazzitelli (1991) as well as the addition of a nonlocal entropy rain term to the convective flux, as in Brandenburg (2016). The latter captures the numerous thin and intense cold downdrafts due to the strong surface cooling and effectively renders the lower CZ into a stably stratified layer, thus establishing a countergradient heat flux (Deardorff, 1966) that underlies the highly asymmetric character of solar convection. However, MLT still suffers from the complexity of characterizing compressible convective turbulence; see also Anders, Lecoanet, and Brown (2019).

The primary goal of MLT is to determine how the nearly adiabatic convection zone accomplishes the transport efficiently. Large-scale simulations of the Sun have attempted to determine $\Lambda(r) = \alpha_{\mathrm{MLT}}\mathcal{H}_p(r)$ backward and obtain a factor α_{MLT}, which is otherwise a free parameter in the theory. We describe the simplest version to illustrate its basic performance.

A striking observation in solar convection is that the temperature gradient in the deep convection region departs little from the adiabatic gradient caused by stratification; see again $\nabla - \nabla_s$ in the inset of Fig. 3(b). The system thus operates close to the marginally turbulent state that is not conducive to generating highly inertial turbulence, except at low Prandtl numbers (Spiegel, 1962). The observation could also imply that turbulence is so well mixed that it homogenizes the gradients subject to the only condition that they be adequate to effect the transport by some kind of gradient transport. MLT can explain this result by starting with the local convective energy flux [which is measured in $\mathrm{J}/(\mathrm{m}^2\,\mathrm{s})$] across any radius r, which is given by $F_{\mathrm{conv}} = \rho(r)V(r)c_p(r)\overline{\delta T}(r)$, where V is the characteristic velocity magnitude across r and $\overline{\delta T}$ is a mean or characteristic temperature deviation from the adiabatic profile at this shell. Over a short distance Λ, one can write

$$\overline{\delta T} = \left(\frac{dT}{dr}\bigg|_s - \frac{dT}{dr}\right)\Lambda =: \Delta_s \Lambda. \tag{28}$$

Now, MLT assumes that this temperature deviation, originating from one shell r in the CZ, is transported to another shell at height $r \pm \Lambda$ without any change and with fixed velocity V, and deposited fully and mixed instantaneously at the new height. One can estimate the deviation from the adiabatic temperature derivative Δ_s that is required to carry the whole radiative flux $L_\odot/(4\pi R_\odot^2)$ by convection. Taking V as the free-fall velocity (see Sec. IV.B for the definition) and setting $\Lambda \sim \mathcal{H}_p$, we have

$$\Delta_s^{3/2} = \frac{L_\odot \sqrt{T}}{4\pi R_\odot^2 \rho c_p \sqrt{g\mathcal{H}_p^4}}. \tag{29}$$

When inserting the values at the geometric mean radius $r_g = \sqrt{r_* R_\odot}$, we get $\Delta_s(r_g) \approx 10^{-10}$ K/m. Since the adiabatic temperature gradient $(dT/dr)_s = -g/c_p \sim \mathcal{O}(10^{-2}\,\mathrm{K/m})$ across the entire CZ, we get $-\Delta_s/(dT/dr)_s \simeq O(10^{-8})$ at a radius $r = r_g$. The conclusion is that $dT/dr \approx (dT/dr)_s$. The precise numerical difference is not important and should not in any case be expected to be constant radially in the CZ, but its smallness indicates that convection in the Sun is extremely delicate; but the small difference between the two gradients is crucial for convection. It is indeed possible to construct an effective temperature difference by

$$\Theta(r) = \int_{r_*}^{r} \Delta_s(\tilde{r})d\tilde{r}. \tag{30}$$

The plot of this profile is displayed in Fig. 5. Such a profile has a gentle variation across the convection region, and the temperature difference that participates in convection is not the difference of nearly 2×10^6 K between the bottom and top of the CZ but about 6000 K. This is the effective temperature difference that enters the definition of the Rayleigh number.

Despite its naivety, MLT has been remarkably successful as an integral component of stellar structure models. Because all scale heights increase with depth, it follows that the mixing length Λ increases into the interior, suggesting with some caveats the existence of large convective cells, the so-called giant cells, in the deeper layers of the CZ with a diameter of $\ell_{\mathrm{GC}} \sim H \sim 2 \times 10^5$ km and a lifetime $\tau_{\mathrm{GC}} \sim 1$ month; see, e.g., Hathaway *et al.* (2000), Miesch *et al.* (2008), and Hathaway, Upton, and Colegrove (2013). Three-dimensional simulations of global convection, performed more and more imaginatively over the past few years by Miesch, Brun, and Toomre (2006), Käpylä *et al.* (2010), Mitra *et al.* (2014), and Hotta, Rempel, and Yokoyama (2015, 2016), describe low Mach number and non-Boussinesq convection in a stratified medium; see also Sec. V. These simulations predict aspects that are not included in MLT (for example, the giant cells), but their identification is not without ambiguity; this ambiguity suggests that the amplitudes of giant cells (if they exist) may be small, posing a challenge to our understanding of deep solar convection.

B. Superadiabatic free-fall velocity

The calculation of the Prandtl numbers in Sec. III.B is relatively straightforward, though it requires technical expertise relating to dissipation mechanisms at the molecular level; see the Supplemental Material (245). The estimate of the Rayleigh and Reynolds numbers across the convection zone is less so because characteristic scales and velocities that enter

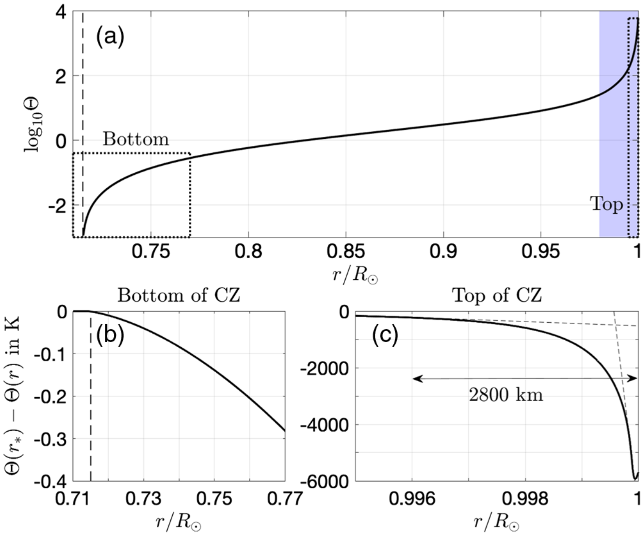

FIG. 5. Effective temperature difference $\Theta(r)$ in kelvin that drives convective motion in the solar CZ. The quantity is calculated by Eq. (30). (a) Full profile across the entire CZ. (b) Enlargement of the bottom of the CZ. (c) Enlargement of the surface layer. Both magnifications are indicated as dotted boxes in (a). The shaded area to the right in (a) stands again for $r \gtrsim 0.98 R_\odot$, where the hydrogen of the solar plasma is only partially ionized. The vertical dashed black lines in (a) and (b) mark $r = r_*$. The intersection point of the two dashed lines in (c) is an estimate for a thermal boundary layer thickness by means of the slope method; see Sec. VII.A.

the estimates are the hardest to obtain accurately. A direct application of the definition of the velocity in Eq. (16) with $H_r = H$ is not as useful as those containing characteristic local scales and velocities, which themselves are associated with local scale heights $\mathcal{H}_k(r)$ of pressure, temperature, or density, $k = \{p, T, \rho\}$. We use here the pressure height scale $\mathcal{H}_p$ because it also enters the superadiabaticity parameter; see the following discussion. In the spirit of MLT, the characteristic velocity is estimated using only the deviations from the adiabatic conditions. The gain in kinetic energy of a fluid parcel is the result of the deviation from the adiabatic profile, i.e., $U_f^2 \sim \varepsilon$, with ε the small parameter that quantifies the deviation from adiabaticity; see, e.g., Lantz and Fan (1999). This specifies the definition of the characteristic free-fall velocity in Eq. (16) and is given by

$$U_f = \sqrt{\varepsilon g_r \mathcal{H}_p} \quad \text{with} \quad \varepsilon = -\frac{\mathcal{H}_p}{c_p}\frac{ds}{dz} = \mathcal{H}_p \frac{\Delta_s}{T} > 0. \tag{31}$$

This relation is a consequence of the first law of thermodynamics $\rho T ds = \rho c_p dT - dp$ and of $ds/dz|_s = 0$. A similar form for the free-fall velocity can be found in Spiegel (1963), where $\Lambda^2/4$ enters the expression for the free-fall velocity instead of $\mathcal{H}_p^2$; see Eq. (31). The free-fall velocity profile in the inset of Fig. 6(a) displays growth from $U_f(r^*) \sim 30\ \mathrm{m\,s^{-1}}$ to $U_f(R_\odot) \sim 3\ \mathrm{km\,s^{-1}}$ at the surface. The latter velocity magnitude is of the same order as that of a minimum vertical velocity that is necessary to compensate for the radiative losses in the granules at the solar surface (Nordlund, Stein, and Asplund, 2009). We note that only at the surface does the free-fall velocity reach magnitudes of the order of the sound speed; the Mach number $M = U_f/c_s \lesssim 10^{-3}$ for most of the CZ, which suggests that the flow is practically incompressible on scales $\ell \ll \mathcal{H}_p$.

C. Rayleigh number

Figure 6(a) shows the variation of the Rayleigh number across the convection layer based on

$$\mathrm{Ra}_\odot(r) = \frac{\rho^2 U_f^2 \mathcal{H}_p^2}{\eta_i^2} \mathrm{Pr}_\odot = \frac{\varepsilon g \rho \mathcal{H}_p^3}{\eta_i \kappa_\gamma}. \tag{32}$$

Even though we take the local pressure scale height in the estimate, the Rayleigh number remains extremely large and does not fall below 10^{18} except close to the surface. Taken together with the fact that low-Prandtl-number convection is known to generate vigorous fluid turbulence [as demonstrated in direct numerical simulations of nonrotating convection by Breuer *et al.* (2004), Mishra and Verma (2010), and Schumacher, Götzfried, and Scheel (2015) as well as rotating convection by Calkins *et al.* (2012)], the conventional wisdom appears to be correct that turbulence levels in the bulk of the CZ are high, thus making it hard to maintain well-organized structures over long periods of time. The Rayleigh numbers are not as large as the preliminary estimates in Sec. I, but there are still some unresolved issues in this estimate.

Toward the surface, the numerical estimates of Fig. 6(a) are not reliable because the transport properties cannot be obtained accurately. Even so, it is clear that the Rayleigh number falls precipitously toward the surface, making it possible for several types of well-organized structures to be maintained in the surface layer, characteristic of convection at low to moderate Rayleigh number. We mention here (before revisiting in Sec. IV.E) that strong rotation provides an alternative reason for large surface structures. For example, Featherstone and Hindman (2016) suggested that supergranules may be surface imprints of interior columnar structures that are influenced by rotation.

D. Fluid and magnetic Reynolds numbers

The variations of the fluid and magnetic Reynolds numbers are summarized in Fig. 6(b), which displays the profiles on the basis of the pressure scale height. The definitions $\mathrm{Re}_f(r) = U_f \mathcal{H}_p/\nu_i$ and $\mathrm{Rm}_f(r) = \mu_0 \sigma_e U_f \mathcal{H}_p$ are used here; see Eqs. (17), (18), and (26). High-Reynolds-number turbulence usually displays approximate similarity in which a characteristic fluctuation velocity, such as the root-mean-square value, scales with the characteristic mean velocity: here the velocity U_f from Eq. (31). One should thus expect rms velocity fluctuations of the order of tens of meters per second in the interior, increasing to a few hundred meters on the surface. The Reynolds stresses, which in kinematic units would typically be of the order of the square of this velocity, have some bearing on determining the organization and long-term survival of structures in the bulk of the CZ. Figure 6(b) shows that Rm_f in the Sun is of the order of 10^{10} in the CZ. Even

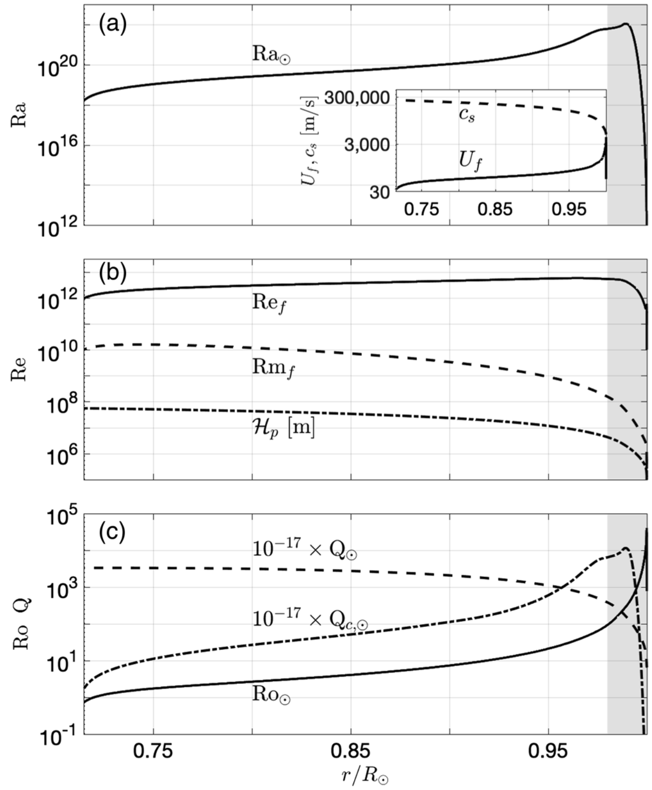

FIG. 6. Variation of Rayleigh, Reynolds, Rossby, and Chandrasehkar numbers across the solar convection zone based on model S. (a) The profile of the Rayleigh number $\mathrm{Ra}_\odot(r)$. Free-fall velocity and Rayleigh numbers are calculated with respect to the pressure scale height. (Inset) Variation of the free-fall velocity U_f [see Eq. (31)] and the adiabatic speed of sound c_s [see Eq. (27)]. (b) Variation of flow and magnetic Reynolds numbers across the CZ. Also shown is the pressure scale height in meters. (c) Variation of Rossby and Chandrasekhar numbers across the CZ. The shaded area to the right in both figures corresponds to $r_i \gtrsim 0.98 R_\odot$ where the hydrogen of the solar plasma is only partially ionized. In (c), we add the Chandrasekhar limit $\mathrm{Q}_{c,\odot} = \mathrm{Ra}_\odot/\pi^2$; see Sec. V.B.

though Rm_f decreases toward the outer parts of the CZ, it is still of the order of 10^6 in the outer shallow convection layer. Such magnetic Reynolds numbers are completely outside our capacity to simulate or replicate in a laboratory experiment. The magnetic fields at such high Rm are likely to be frozen into the flow and move with it; thus, magnetic fields can persist for an extremely long time as they rise from the tachocline; see Sec. IV.E. Only the large local gradients on the edge tend to smooth out. However, $\mathrm{Rm}_f < \mathrm{Re}_f$, so a rising or descending plume will maintain its integrity for longer distances than its magnetic content.

E. Rossby and Chandrasekhar numbers

Rotation and dynamo action are the physical processes that are connected to the next two dimensionless parameters, the Rossby and Chandrasekhar numbers. Figure 6(c) shows the solar Rossby number profile $\mathrm{Ro}_\odot(r) = U_f/(2\mathcal{H}_p\Omega)$ if we take the characteristic rotation time to be that of the equator with $\Omega^{-1} \sim 27$ days, the characteristic length with $\mathcal{H}_p$ from Fig. 2(c), and the corresponding free-fall velocity U_f from the inset of Fig. 6(a). We get local Rossby numbers $\mathrm{Ro}_\odot$ that vary from $\mathcal{O}(1)$ at the bottom to $\mathcal{O}(10^3)$ near the surface, which indicates that the Sun is to a first approximation a slowly rotating star. They are larger than those inferred via helioseismically measured surface flows that start at the surface with $\mathrm{Ro}_\odot \approx 5$ and decrease to 0.2 at a depth of $z \approx 3 \times 10^4$ km (Greer, Hindman, and Toomre, 2016). One may be tempted to conclude that rotation plays only a modest role for the solar dynamics, except perhaps close to the bottom of the CZ. This statement needs to be parsed further because rotation affects phenomena at different scales differently: granules are essentially unaffected by rotation with $\mathrm{Ro}_\mathrm{G} = v_\mathrm{G}/(2\ell_\mathrm{G}\Omega) \gtrsim \mathcal{O}(10^3)$ and supergranules perhaps only modestly with $\mathrm{Ro}_\mathrm{SG} = v_\mathrm{SG}/(2\ell_\mathrm{SG}\Omega) \gtrsim \mathcal{O}(10)$, although their capacity to support prograde waves suggests that rotation has an impact (Gizon, Duvall, and Schou, 2003). Giant cells (which are thought to circulate deep into the CZ) strongly vary with $\mathrm{Ro}_\mathrm{GC} = v_\mathrm{GC}/(2R_\odot\Omega) \sim \mathcal{O}(10^{-1})$. These magnitudes are taken from Hathaway, Upton, and Colegrove (2013) and are listed in the caption of Fig. 1.

The Sun, presumably a faster rotating star once, has lost some of its angular momentum via the solar wind at the surface; some of this loss may be attributed to the perennial radiation [by the so-called Poynting-Robertson effect, which is the process by which solar radiation drags the dust particles through the shear in the thin region of the Sun's photosphere, as discussed by Cunnyngham *et al.* (2017)]. This scenario suggests a fast-rotating core and a slowly rotating envelope, as is true of the solid core. The evidence from helioseismology is that the radiative interior is rotating nearly uniformly at a rate between the polar rate of ~1/34 days and the equatorial one of ~1/27 days. The differential rotation between the equator and the poles, sustained by the extraction of angular momentum from the radiative interior and subsequent redistribution by turbulent stresses and latitudinal thermal gradients, plays an important role for the solar magnetic dynamo.

Large amplitude magnetic flux emerges prominently in the form of coherent loops (Török and Kliem, 2005) into the photosphere and solar corona, thus forming bipolar pairs of sunspots at the solar surface close to the equator. Their variation in number and magnetic field strength in a nearly 22-yr cycle suggests a global flux transport-based dynamo that converts toroidal magnetic flux into poloidal magnetic flux and vice versa in a quasiregular fashion; see also Ossendrijver (2003), Solanki, Inhester, and Schüssler (2006), Dikpati and Gilman (2007), Charbonneau (2010), Karak *et al.* (2014), Brun and Browning (2017), and Moffat and Dormy (2019) and our discussion in Sec. V. Estimates of the maximum magnitude of the magnetic induction field, which rises in the form of coherent flux tubes through the CZ, give $B \lesssim 10$ T; see also Choudhuri and Karak (2009). Although it is still unclear how such strong fields can be generated within the Sun, the property of spatiotemporal intermittency (Sreenivasan and Antonia, 1997) makes such large amplitudes plausible locally. Figure 6(c) plots the Chandrasekhar number $Q_\odot(r) = \sigma_e B_0^2 \mathcal{H}_p^2/\eta_i$, with a typical amplitude of $B_0 \sim 0.1$ T, in correspondence with a magnetic network pattern that is tied to supergranulation shown by Ossendrijver (2003).

The existence of a "fossil" magnetic field as a remnant from the early evolution stage of the Sun cannot be excluded, but there is no direct and convincing evidence of this, as discussed by Ossendrijver (2003) and Solanki, Inhester, and Schüssler (2006). The existence of the thin tachocline layer indicates that such a magnetic field would be enclosed in the uniformly rotating radiation zone.

At present, the detailed interplay between convection, rotation, and magnetic fields is not fully understood. Some simulations [see, e.g., Brun and Toomre (2002) and Balbus *et al.* (2009)] indeed show a strong and sustained differential rotation, not unlike helioseismic observations. Other simulations do not seem to produce similarly consistent results; see Hanasoge, Hotta, and Sreenivasan (2020).

F. Flux-based Nusselt number estimate at the solar surface

The radiation released with a surface luminosity $L_\odot = L(r = R_\odot) = 3.828 \times 10^{26}$ W causes an extremely strong radiative cooling, thought to be a major driver of solar convection. The known value of $L_\odot$ allows us to estimate a Nusselt number at the top of the CZ. The dimensionless Nusselt number Nu is defined as the ratio of the total heat flux to the diffusive one and is given on average by

$$\mathrm{Nu} = \frac{q_{\mathrm{total}}}{q_{\mathrm{diff}}} = \frac{L_\odot / 4\pi R_0^2}{-k_\gamma(R_0)\Gamma_s(R_0)} \approx 1.31 \times 10^6, \qquad (33)$$

with $R_0 = 0.99 R_\odot$ and the adiabatic lapse rate $\Gamma_s = dT/dr|_s$. One might ask how this estimate for the Nusselt number is related to the local Rayleigh numbers obtained in Sec. IV.C. The local value at $r = R_0$ is $\mathrm{Ra} \approx 10^{22}$ according to Fig. 6(a). With no knowledge of a possible existence of an ultimate regime in stellar convection and lacking completely reliable Rayleigh number estimates, we cannot make extrapolations of scalings Nu (Ra); see, e.g., Chillà and Schumacher (2012) for more details.

V. SIMULATIONS OF SOLAR CONVECTION

The variation of thermodynamic properties and the gas composition between the top and bottom of the CZ renders solar convection highly non-Boussinesq. Even though only small departures from the large adiabatic gradients of temperature and density participate in solar convection, these small departures occur in the background of large stratification. This combined problem has been addressed only in numerical simulations, which we now summarize. Simulations have been an important tool for building intuition about the highly complex convection dynamics in the Sun.

Yet, as stated in Sec. I, none of the numerical approaches are currently able to simulate the full set of equations (1)–(6). None of them can approach the range of parameters discussed in Secs. III and IV, nor can they resolve all scales of motion and include the impact of the highly intermittent small-scale turbulence on eddy viscosity and diffusivity. As a rule, simulations of deep and surface convection rely mostly on implicit or prescribed numerical diffusion, with the physical subgrid scale (SGS) models the exception to this rule (Nelson *et al.*, 2014; Kitiashvili *et al.*, 2015). Even with the finest vertical grid resolutions, such as $h_z = 48$ km at the solar surface in Hotta, Iijima, and Kusano (2019) or $h_z \gtrsim 6$ km in Kitiashvili *et al.* (2012), one might be 6 orders of magnitude away from the Kolmogorov scale; see the estimates in Table I. Figure 7 groups the simulations into (i) penetrative convection into the tachocline, (ii) deep convection in the bulk, and (iii) compressible convection in the surface shear layer. Some simulations bridge these three regions, just as the physical mechanisms themselves bridge across them; examples are shown in Fig. 8. Simulations of penetrative convection at the bottom of the CZ were typically conducted in a local Cartesian geometry applying the fully compressible equations; see Tobias *et al.* (1998), Brummell, Cline, and Cattaneo (2002), Kitiashvili *et al.* (2016), and Käpylä *et al.* (2017), and see also Fig. 8(d) for a vertical cut snapshot by Hotta (2017). The Supplemental Material (245) contains a summary of important families of approximate equations solved numerically; it also contains a description of numerical methods and the approximations implied at that stage.

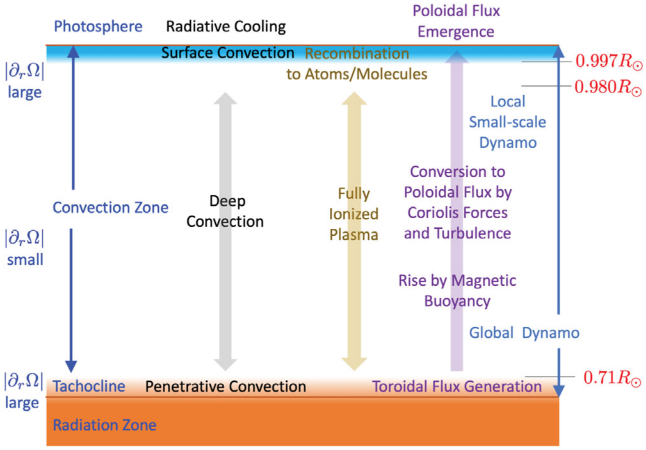

FIG. 7. Interaction and coexistence of physical processes with turbulent convection regimes in the solar convection zone. A depth of $z = 2 \times 10^3$ km corresponds to $r \approx 0.997 R_\odot$, and $z = 1.4 \times 10^4$ km corresponds to $r \approx 0.98 R_\odot$. At the top and bottom differential rotation is large in magnitude compared to that in the bulk.

Global simulations of deep solar convection in spherical shell geometry apply either the anelastic approximation to Eqs. (1)–(6), such as in the anelastic spherical harmonics code by Clune *et al.* (1999) and the Eulerian–semi-Lagrangian fluid solver by Prusa, Smolarkiewicz, and Wyszogrodski (2008), or the reduced sound speed technique that rescales the continuity equation, such as in a higher-order finite difference solver by Hotta, Rempel, and Yokoyama (2016); see the Supplemental Material (245) for details on these global simulations and the anelastic limit. The top boundary in these studies is at $r \approx 0.98 R_\odot$; see Fig. 7. Applications aim toward (1) a better understanding of the global solar dynamo in combination with the 22-yr sunspot cycle (Nelson *et al.*, 2014; Hotta, Rempel, and Yokoyama, 2016); (2) the reproduction of the complex differential rotation profiles that vary in radius and latitude in the Sun (Brun and Toomre, 2002); (3) the interaction of the

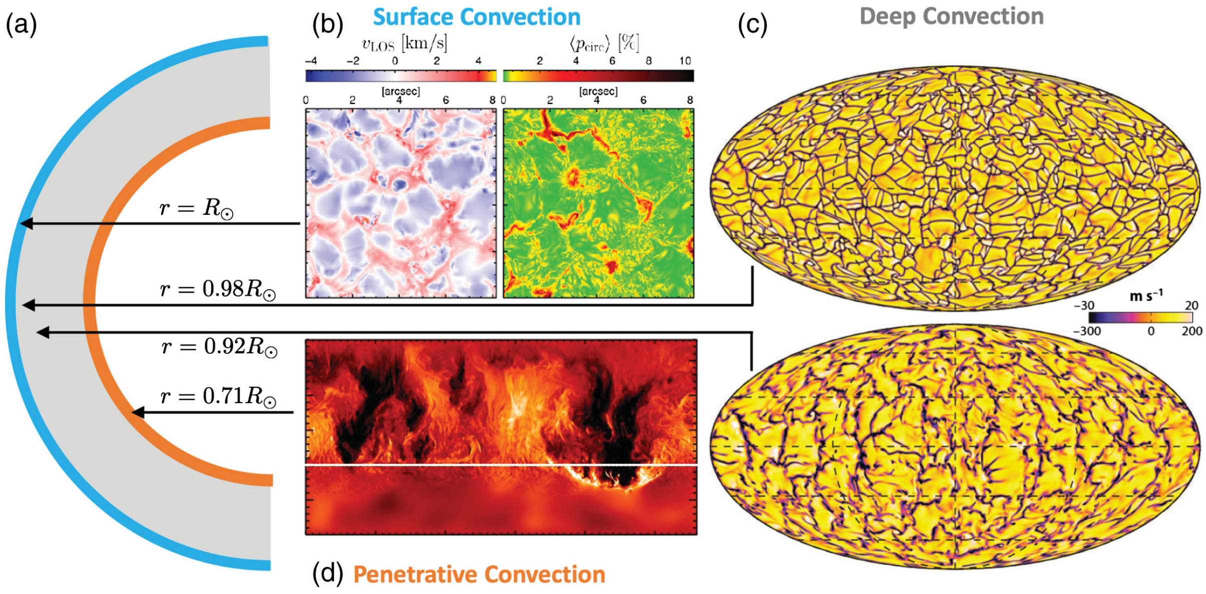

FIG. 8. Numerical simulations of solar convection. (a) Schematic of the solar convection zone with highlighted surface layer (outer thick line) and tachocline (inner thick line). (b) Simulations of surface convection from Riethmüller *et al.* (2014). Left panel: vertical (line of sight) velocity component $v_{\rm LOS}$. Right panel: mean circular polarization $\langle p_{\rm circ}\rangle$ of the Fe I line at 5250.2 Å as a measure of the magnetic field strength. One arc second corresponds to 727 km. (c) Radial velocity at (top panel) $r = 0.98R_\odot$ and (bottom panel) $r = 0.92R_\odot$ showing upflows and downflows by Miesch *et al.* (2008). (d) Penetrative convection into the tachocline by Hotta (2017). The figure shows contours of the vertical velocity component in a vertical cross section. The white line marks the border between the convection and radiation zones.

CZ with the tachocline via the modification of the thermal boundary conditions at the bottom, as in Miesch, Brun, and Toomre (2006) and Guerrero *et al.* (2016); and (4) the numerical search for giant convection cells, as reported by Miesch *et al.* (2008) and Bessolaz and Brun (2011). As seen in Fig. 8(c), solar convection is in line with a global network of highly asymmetric and strongly height-dependent upflows and downflows: radiative top cooling generates thin downwelling thermal plumes that sink into a highly stratified bulk. Effective Prandtl and Rayleigh numbers on the basis of subgrid scale eddy dissipation lead, for example, to $\mathrm{Pr}_t = 0.25$ and $\mathrm{Ra}_t = 3 \times 10^4$ in Miesch *et al.* (2008). (5) Other numerical simulations, such as those by Passos, Charbonneau, and Miesch (2015), focus on the weak meridional circulation (Rüdiger, 1989; Gough and McIntyre, 1998), the conveyor-belt-type circulation that seems essential for bringing poloidal magnetic flux from the tachocline to the poles.

At this point, it might be instructive to give a brief sketch of current global solar dynamo models. (i) Babcock-Leighton flux transport dynamos (Babcock, 1961; Leighton, 1964; Miesch and Toomre, 2009) assume that toroidal magnetic flux is generated by strong differential rotation (the so-called Ω effect) in the tachocline, the high-shear layer that separates the CZ from the stably stratified and rigidly rotating radiation zone; see also Fig. 7. Therefore, poloidal magnetic flux is brought by plume overshoots and a weak meriodional circulation from the CZ into the tachocline, a process denoted as magnetic pumping (van Ballegooijen, 1982). Tachocline dynamo action might also proceed in combination with magnetorotational and shear instabilities (Balbus and Hawley, 1991; Kagan and Wheeler, 2014; Rincon, 2019). Once strong enough, toroidal magnetic flux tubes become susceptible to magnetic buoyancy, leave the tachocline into the CZ, and are now additionally subject to twisting by rotation and shredding by rising turbulence due to convection (Zwaan, 1978). Toward the near-surface layer (which again displays strong differential rotation) the most coherent and strongest toroidal flux is thus reconverted into poloidal flux; the latter leaves the solar interior either as a highly intermittent smaller-scale magnetic field between granules and supergranules or in the form of bigger coronal loops from sunspot pairs. (ii) Interface dynamos work somewhat differently (Parker, 1955, 1993). The toroidal magnetic flux generated from the tachocline is converted into poloidal magnetic flux by turbulent electromotive forces in the CZ, the so-called α effect (Steenbeck, Krause, and Rädler, 1966; Rüdiger, 1989). The dynamo might then take on the character of a surface wave that eventually manifests as a magnetic wreath, as in the simulations of Nelson *et al.* (2014). It is thought that in combination with this global magnetic cycle a small-scale dynamo is at work in connection with the stronger turbulence in the upper CZ, as investigated by Kitiashvili *et al.* (2015). Augustson, Brun, and Toomre (2019) classified a record of recent full-convection-zone dynamo simulations [among them Strugarek *et al.* (2018) and Viviani *et al.* (2018)] with respect to their ratio of magnetic to kinetic energy as a function of Pm and Ro by

$$\frac{\langle \boldsymbol{B}^2\rangle}{\langle \rho \boldsymbol{u}^2\rangle \mathrm{Pm}} \approx a + \frac{b}{\mathrm{Ro}}, \tag{34}$$

with the fit parameters $a = 0.053 \pm 0.007$ and $b = 0.062 \pm 0.010$. The relation describes a crossover from a Ro-independent ratio for slowly rotating stars to a ratio that grows linearly with Ro^{-1} for rapidly rotating stars. The range of accessible Pm is, however, rather small and differs strongly from the value in the Sun.

Deep convection simulations on the small-scale dynamo were also carried out in a local Cartesian geometry such as in Hotta, Rempel, and Yokoyama (2015) for a horizontal domain $R_\odot \times R_\odot$ and a significantly higher grid resolution, as small as 350 km horizontally and similar depth ranges to those discussed earlier. The joint action of magnetic buoyancy, Coriolis forces, and tube curvature converts the toroidal magnetic field into a poloidal magnetic field; see, e.g., Caligari, Moreno-Insertis, and Schüssler (1995). Flux tubes are eventually released inside the upwelling regions between granules and supergranules (Solanki, Inhester, and Schüssler, 2006; Langfellner, Gizon, and Birch, 2015b).

Simulations of surface convection have to include three physical aspects that can be neglected or simplified for deep or penetrative convection. These are compressibility, radiative transport beyond the gray approximation (for which absorption and emission do not depend on wavelength λ), and partial ionization of chemical species. Code packages by Vögler *et al.* (2005), Gudiksen *et al.* (2011), Freytag *et al.* (2012), Magic *et al.* (2013), and Wray *et al.* (2015) include these physical processes and reach to depths of a few thousand kilometers; see Fig. 7. The Supplemental Material (245) provides details of simulation models and methods. These studies partly include the photospheric dynamics and use tabulated state variables for the most abundant elements (Rogers and Iglesias, 1992) to provide precise opacities; see Sec. III.A. Thus, the complexity and research focus here shifts from global turbulent convection processes to impacts of radiation transport and changes in the state of ionization, and it centers on the local dynamics of (1) granules [see Fig. 8(b)] and supergranules (Jacoutot *et al.*, 2008; Riethmüller *et al.*, 2014), (2) sunspot formation (Rempel, 2012), (3) the small-scale dynamo near the surface (Hotta, Rempel, and Yokoyama, 2015), (4) the emergence of magnetic flux in the photosphere, resulting in coronal heating (Gudiksen *et al.*, 2011), (5) the excitation of strong density perturbations and acoustic waves by vortex pairs of opposite signs (Kitiashvili *et al.*, 2011), and (6) the direct comparison of spectral lines from observations of the quiet Sun by Hathaway *et al.* (2015) to those obtained in radiative magnetohydrodynamic simulations by Kitiashvili, Couvidat, and Lagg (2015). These simulations are typically conducted in local Cartesian geometries and have the advantage of being directly compared to optical observations (Nordlund, Stein, and Asplund, 2009; Roudier *et al.*, 2016), in strong contrast to deeper convection results.

Besides acoustic waves, internal waves appear in the zone of strongest stratification close to the surface. Helioseismology has now been able to detect low-frequency g modes in the interior (Appourchaux *et al.*, 2010), as well as surface Rossby waves (Löptien *et al.*, 2018). Internal gravity waves are also thought to have some effect on the structure of the Sun's chromosphere (Vigeesh, Jackiewicz, and Steiner, 2017). However, the connection between these modes and deep convection is at best imperfectly understood.

Finally, simpler models are used when more emphasis is given to certain aspects of turbulent convection processes. These are, for example, the compressible nonmagnetic convection runs in large domains with $\Gamma = 42$ to analyze mesoscale surface convection, in particular, granule dynamics (Rincon, Lignièeres, and Rieutord, 2005), the surface-cooling-driven convection without the $\boldsymbol{B}$ field (Cossette and Rast, 2016), small-scale dynamos in magnetohydrodynamic turbulence in cubes with periodic boundary conditions (Schekochihin *et al.*, 2007; Singh, Rogachevskii, and Brandenburg, 2017), and the RBC models with temperature-dependent diffusivity (Shcheritsa, Getling, and Mazhorova, 2018).

VI. LESSONS FROM EXPERIMENTS AND NUMERICAL SIMULATIONS OF RAYLEIGH-BÉNARD CONVECTION

A. Limited analogy to RBC

In spite of the superficial resemblance, in both structure and dynamics, between solar convection and the RBC in the laboratory and simulations, the two cases differ in important respects. For example, the boundary conditions for the CZ in the Sun correspond to constant heat flux with no solid surfaces, unlike the case of constant temperature in RBC; convective parameters in the Sun are extreme; large scales are affected by rotation, which presumably sustains various structures (e.g., stretched out giant cells and the so-called banana cells); interesting phenomena such as differential rotation (which we have already encountered); and meridional circulation, which consists of a weak poleward motion of the high-momentum fluid from the equator near the surface and a corresponding return from the poles near the base of the CZ (Rüdiger and Kitchatinov, 1996; Gough and McIntyre, 1998; Miesch *et al.*, 2012), have no analogs in RBC. While the fluid is fully ionized over the bulk of the CZ, it is only partially ionized in the outer layer of the CZ, which makes the fluid in that layer highly complex. Laboratory experiments make special efforts to respect the so-called Boussinesq approximation (according to which the effect of temperature variations are felt only through gravitational effects), and numerical RBC simulations almost always assume that this approximation will hold. Thus, no laboratory experiment or numerical RBC simulation has (or will) come close to replicating all the conditions in the Sun, so the insights that can be carried over from the laboratory to the Sun are necessarily qualitative. Yet, it is useful to describe laboratory flows and simulations here, if only to provide a useful contrast while also setting a plausible framework for further discussion. The Supplemental Material (245) includes the derivation of the appropriate equations from the full compressible equations of Sec. I.

B. Heat transport

Laboratory experiments on RBC have pushed toward increasingly high Rayleigh numbers, keeping in mind geophysical and astrophysical contexts. Even though the questions that they address have distinct characters, their one goal has been to arrive at definitive results under controlled conditions, with the expectation that they may have general qualitative relevance in more general circumstances.

RBC experiments have been carried out using a fluid held in a container with nonconducting sidewalls and perfectly conducting bottom and top walls that are heated from below and cooled from above so that all of the heat from the bottom wall is transferred through the fluid to the top wall. The Boussinesq approximation (Verma, 2018) assumes a linear temperature dependence of the mass density $\rho(p,T)\boldsymbol{g}\simeq -g_r\rho_r[1-(T-T_r)/T_r]\boldsymbol{e}_z$ and simplifies Eqs. (1)–(3) for $\boldsymbol{B}=0$, constant material parameters, and $g_r=g$ to

$$\boldsymbol{\nabla}\cdot\boldsymbol{u}=0, \tag{35}$$

$$\rho\frac{D\boldsymbol{u}}{Dt}+2\rho(\boldsymbol{\Omega}\times\boldsymbol{u})=-\boldsymbol{\nabla}p+\eta\boldsymbol{\nabla}^2\boldsymbol{u}+\rho g\frac{T-T_r}{T_r}\boldsymbol{e}_z, \tag{36}$$

$$\frac{DT}{Dt}=\kappa\boldsymbol{\nabla}^2T. \tag{37}$$

An important question concerns the amount of heat and momentum that is transported across the fluid for a given temperature difference maintained between the bottom and top walls. Heat is transported purely by molecular conduction if the temperature difference is small, but the fluid begins to move and enhance the heat transport for higher temperature differences. The buoyancy caused by the temperature difference is balanced by the smearing effects of diffusion and viscosity, with the ratio of the former to the latter being the Rayleigh number Ra (see Sec. I); the larger the Rayleigh number, the larger the effective temperature difference. The Nusselt number Nu measures the enhancement of heat transport, and the flow Reynolds number Re [see Eq. (18)] measures the momentum transport. One goal of convection studies is to discover how Nusselt and Reynolds numbers scale with the Rayleigh number for RBC with smooth walls in a particular working fluid, i.e.,

$$\mathrm{Nu}=q_{\mathrm{tot}}/q_{\mathrm{diff}}=f(\mathrm{Ra},\mathrm{Pr},\Gamma), \tag{38}$$

$$\mathrm{Re}=u_{\mathrm{rms}}\mathrm{Re}_f/U_f=g(\mathrm{Ra},\mathrm{Pr},\Gamma). \tag{39}$$

The quantity u_{rms} is the root-mean-square velocity and $\Gamma=L/H$ is the aspect ratio of the container with side length (or diameter) L. Much is known about this flow configuration [see, e.g., Castaing *et al.* (1989), Goldstein, Chiang, and See (1990), Grossmann and Lohse (2000), Niemela *et al.* (2000), Niemela and Sreenivasan (2006), Ahlers, Grossmann, and Lohse (2009), Grossmann and Lohse (2011), Chillà and Schumacher (2012), and Urban *et al.* (2014)], though most of the information at high Rayleigh number has been gathered for convection layers that are not shallow, i.e., $\Gamma\lesssim 1$.

The question of interest in solar convection is just the opposite of Eqs. (38) and (39): we know the amount of thermal energy transported across the convection layer and want to understand the turbulence structure that enables the prescribed heat transport to occur. It is in this context that one needs to possess the knowledge of the flow parameters, the transport coefficients, the boundary layers, etc. There have been only a small number of studies that prescribe the heat flux (instead of wall temperatures), see the direct numerical simulation (DNS) studies of Verzicco and Sreenivasan (2008) and Johnston and Doering (2009), but the general conclusion from those studies is that the flow structure in the bulk is extremely similar to the constant temperature case modulo a transformation of the Rayleigh number.

C. Role of boundary layers

Rayleigh numbers in these laboratory studies for $\mathrm{Pr}\simeq 1$ are high by nominal instability criteria, but the only studies that have a modest overlap with Fig. 6(a) are those of Niemela *et al.* (2000) and Niemela and Sreenivasan (2003a), which suggests that the Nusselt number varies essentially as the $1/3$ power of the Rayleigh number up to $\mathrm{Ra}=10^{17}$. While it would be highly desirable to get independent confirmation (or unambiguous refutation) of these results, the general inference from these data is that the boundary layers, no matter how thin, continue to play an important role in heat transport. There are proposals by Kraichnan (1962), Chavanne *et al.* (1997), and Grossmann and Lohse (2011) that the power-law exponent approaches $1/2$ (modulo Prandtl number effects) toward the so-called ultimate regime when the boundary layer effects vanish, but there is no unequivocal verification that this occurs in smooth-wall flows (Siggia, 1994; Niemela and Sreenivasan, 2003a; Niemela, Babuin, and Sreenivasan, 2010; Ahlers *et al.*, 2012; He *et al.*, 2012; Urban *et al.*, 2014, 2019; Zhu *et al.*, 2018; Doering, Toppaladoddi, and Wettlaufer, 2019; Zhu, Mathai *et al.*, 2019). Three-dimensional DNS has advanced in recent years, and we may mention DNS of RBC at a unity Prandtl number at $\Gamma=1/10$ up to $\mathrm{Ra}=10^{15}$ by Iyer *et al.* (2020), in air at $\mathrm{Pr}=0.7$ by Stevens, Lohse, and Verzicco (2011) at $\Gamma=0.23$, which currently accesses $\mathrm{Ra}=10^{14}$, and in $\Gamma=1/2$ for $\mathrm{Ra}\le 2\times 10^{12}$, and by Shi, Emran, and Schumacher (2012) for $\Gamma=1$, $\mathrm{Pr}=0.7$, and $\mathrm{Ra}\le 3\times 10^{10}$. The cumulative conclusion seems to favor the continued importance of thin boundary layers.

On the other hand, the power law of $\mathrm{Nu}\sim\mathrm{Ra}^{1/2}$ does seem to occur when the boundary layers are absent in the experiments either because of a chimneylike configuration by Gibert *et al.* (2006) and Cholemari and Arakeri (2009) or because the heating is accomplished purely by body forces, such as radiative forces given by Lepot, Aumaitre, and Gallet (2018) and Bouillaut *et al.* (2019), so that boundary layers do not form. And there are indications that the half-power law is also approached when the walls are rough, as in the two-dimensional DNSs by Toppaladoddi, Succi, and Wettlaufer (2017) and Zhu, Stevens *et al.* (2019). The structure of these flows seems to differ in detail from the case of smooth wall-bounded convection.

D. Boundary conditions for the Sun

As just discussed, RBC studies show that the existence of solid boundaries makes a difference to the heat transport law and the turbulence structure. The convection boundaries in the Sun are evidently not solid to either side of the CZ, but steep changes in the adiabatic temperature gradient at the base of the CZ significantly restrict free movement of plasma across this layer, though there can be small-scale penetrative convection at the tachocline, which is thought to play a critical role in stellar rotation spin-down. In fact, measuring the depth of penetration is an active area of research in helioseismology and asteroseismology; see, e.g., Christensen-Dalsgaard (2002)

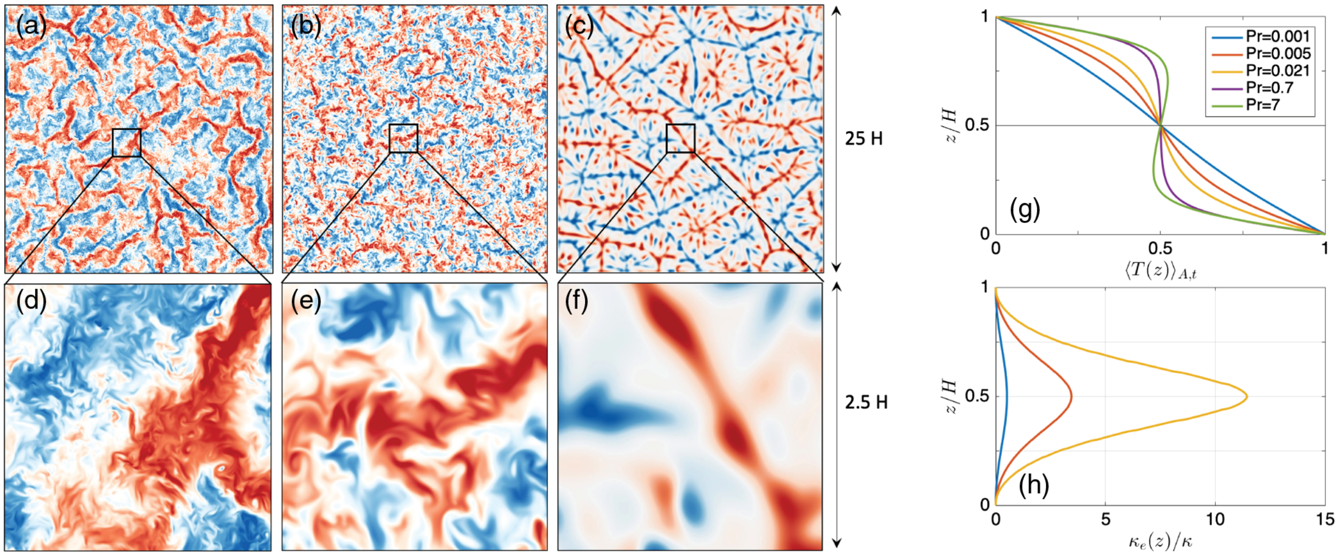

FIG. 9. Snapshots of the vertical velocity component u_z/U_f from direct numerical simulations of Rayleigh-Bénard convection (RBC) at $\mathrm{Ra} = 10^5$ in a large-aspect-ratio closed cell with $L/H = 25$. Length L is the extension of the square cross section. (a) Prandtl number $\mathrm{Pr} = 0.001$, which results in a bulk Reynolds number $\mathrm{Re} = u_{\mathrm{rms}}\sqrt{\mathrm{Ra}/\mathrm{Pr}}/U_f = 4810$. The color scale from blue to red covers $u_z/U_f \in [-0.8, 0.8]$. The three-dimensional computations in (a) and (d) were conducted with a grid resolution of $9600^2 \times 640$ points, applying a code by Krasnov, Zikanov, and Boeck (2011). (b) Convection in air with $\mathrm{Pr} = 0.7$ results to $\mathrm{Re} = 92$. Here $u_z/U_f \in [-0.4, 0.4]$. (c) Convection in water at $\mathrm{Pr} = 7$. This RBC flow results in $\mathrm{Re} = 11$. Here $u_z/U_f \in [-0.2, 0.2]$. (d)–(f) Magnifications of (a)–(c). Data of the two larger Prandtl numbers are from Pandey, Scheel, and Schumacher (2018). (g) Corresponding mean temperature profiles at $\mathrm{Ra} = 10^5$ as a function of Pr becoming nearly linear for $\mathrm{Pr} = 0.001$. (h) Eddy diffusivity profiles $\kappa_e(z)$ for the three lowest corresponding Prandtl numbers.

and Christensen-Dalsgaard, Gough, and Knudstrup (2018). Nevertheless, all large-scale motions are restricted at the base, resulting in a plausible analogy with an impermeable surface when convective overshoots into the tachocline are neglected. Such overshoots cause a deviation from the Boussinesq approximation of RBC, alter the dynamics, and induce different thicknesses of the top and bottom boundary layers (Couston *et al.*, 2017; Toppaladoddi and Wettlaufer, 2018). Similarly, at the top of the convection region, steep gradients in temperature and density within the near-surface convection region endow it with impermeable boundary-like properties.

E. Low-Prandtl-number effects

We have seen that the Prandtl number of the fluid is extremely small everywhere in the CZ. Even excellent thermal conductors such as liquid mercury, gallium, and sodium possess Prandtl numbers that are several orders of magnitude larger than that of the solar plasma. Glazier *et al.* (1999) obtained $\mathrm{Ra} \le 10^{11}$ in liquid mercury for $\mathrm{Pr} = 0.021$ in a cell with $\Gamma = 1/2$. Khalilov *et al.* (2018) reached in liquid sodium $\mathrm{Ra} = 1.4 \times 10^7$ at $\mathrm{Pr} = 0.0094$ and $\Gamma = 1$. Both works give the highest Grashof numbers Gr in small-Prandtl-number studies with liquid metals. The DNS reported by Scheel and Schumacher (2017) reached $\mathrm{Ra} = 4 \times 10^8$ for mercury at $\mathrm{Pr} = 0.021$ and $\mathrm{Ra} = 10^7$ for liquid sodium at $\mathrm{Pr} = 0.005$ in closed cylindrical cells of aspect ratio 1 (currently advancing to $\mathrm{Ra} = 5 \times 10^7$). The global heat transport follows $\mathrm{Nu} = A\mathrm{Ra}^{\beta}$, where β is slightly larger than 1/4 [as expected for low-Ra flows; see, e.g., Busse and Clever (1981)]. Taken together, we may conclude that no direct experience exists with high-Rayleigh-number RBC with exceedingly low Prandtl numbers.

Even so, we can make some qualitative remarks on the effect that extremely low Prandtl numbers might have on the velocity fluctuations at high Ra. In Fig. 9, we display results for a DNS of RBC in an extended domain of $\Gamma = 25$ for an extremely small value of $\mathrm{Pr} = 10^{-3}$, compared to the structure of the vertical velocity components in RBC flows at the same Ra, but in air $\mathrm{Pr} = 0.7$ and water $\mathrm{Pr} = 7$. A decrease from $\mathrm{Pr} = 0.7$ to 10^{-3} causes an increase of the bulk Reynolds number by a factor of 50, thus making the flow more inertial in effect; also shown in Fig. 9 are the nontrivial structural changes in the flow. On the other hand, the Nusselt number is not significantly enhanced beyond unity for $\mathrm{Pr} = 10^{-3}$, confirming an increasingly inefficient turbulent heat transport when Pr drops, as shown by the mean temperature profiles in Fig. 9(g). For $\mathrm{Pr} = 10^{-3}$, the profile is nearly linear and thus $\mathrm{Nu} \approx 1$. These studies confirm previous DNS analyses by Breuer *et al.* (2004) and Schumacher, Götzfried, and Scheel (2015) that reported an extension of the turbulent cascade and thus of more vigorous fluid turbulence for decreasing Pr. Recent simulations in the solar context with flux boundary conditions by Orvedahl *et al.* (2018) also suggest that free-fall velocity is quickly attained and fluid inertia becomes increasingly important when the Prandtl number decreases. These studies also confirm that, despite the increase of turbulent inertia and of the range of eddy scales, the effective turbulent thermal diffusivity κ_e at these extremely low molecular Prandtl numbers might be decreased significantly as Pr

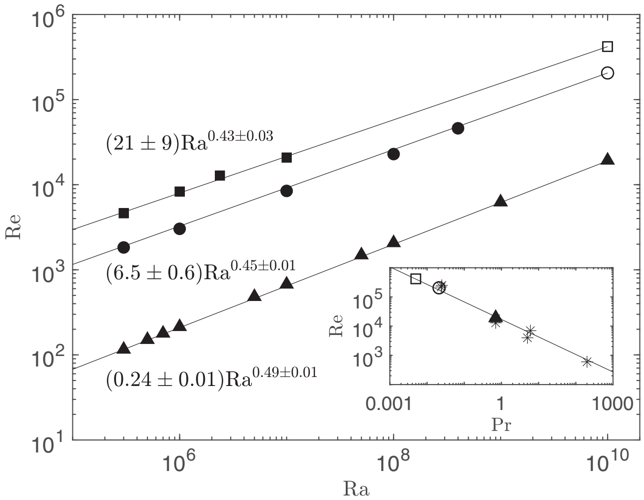

FIG. 10. Reynolds number vs Rayleigh number at $\mathrm{Pr} = 0.005$ (squares), $\mathrm{Pr} = 0.021$ (circles), and $\mathrm{Pr} = 0.7$ (triangles) with corresponding scaling laws. Open symbols are extrapolations to $\mathrm{Ra} = 10^{10}$. Data and fits are from Scheel and Schumacher (2017). Inset: extrapolated and measured data at $\mathrm{Ra} = 10^{10}$ vs Pr. The solid line stands for $\mathrm{Re} = 1.7 \times 10^4\ \mathrm{Pr}^{-0.6}$. Asterisks are from Niemela and Sreenivasan (2003a).

decreases. Here κ_e is obtained by a simple Boussinesq ansatz $\langle u_z' T' \rangle_{A,t} = -\kappa_e(z)\partial\langle T(z)\rangle_{A,t}/\partial z$. In Fig. 9(h), the profiles $\kappa_e(z)/\kappa$ are therefore displayed for the three lowest Prandtl numbers in the simulation series.

Finally, Fig. 10 summarizes the dependence of the Reynolds number Re [see Eq. (39)] on Ra for different values of Pr for RBC in closed cylindrical cells. The inset collects data that are measured at, or extrapolated to, $\mathrm{Ra} = 10^{10}$. They follow $\mathrm{Re} \approx 1.7 \times 10^4\,\mathrm{Pr}^{-0.6}$, which results, after using Eq. (39), in a scaling of the bulk rms velocity $u_{\mathrm{rms}}/U_f = 0.17 \times \mathrm{Pr}^{-1/10}$. Thus, $u_{\mathrm{rms}} \approx 0.17 U_f$ at $\mathrm{Pr} \sim 1$, $0.34 U_f$ at $\mathrm{Pr} \sim 10^{-3}$, and $0.68 U_f$ at a solar value of $\mathrm{Pr} \sim 10^{-6}$. This estimate again underlines the increasingly vigorous fluid turbulence with decreasing Prandtl number at fixed Ra.

F. Effect of rotation

Rotation of the convection layer about the vertical axis suppresses the onset of convection and constrains turbulence for sufficiently large angular rotation Ω (Rossby, 1969; Plumley and Julien, 2019). The DNSs by Oresta, Stringano, and Verzicco (2007), Stevens, Clercx, and Lohse (2010), Weiss *et al.* (2010), and Horn and Shishkina (2015) of rotating turbulent Rayleigh-Bénard convection show, however, no significant enhancement of the heat transport in comparison to the nonrotating case, an effect that becomes even weaker as Ra grows and/or Pr decreases. This was confirmed in low-Rossby-number experiments by Kunnen *et al.* (2011) and Ecke and Niemela (2014); see also Ahlers, Grossmann, and Lohse, 2009. Further, in flows with $\mathrm{Pr} \ll 1$, Ekman pumping becomes unimportant compared to those at $\mathrm{Pr} \sim 1$ (Stevens, Clercx, and Lohse, 2010; Horn and Shishkina, 2015). Depending on Pr, Horn and Shishkina (2015) identified different regimes of rotating RBC by comparing the poloidal and toroidal energies of the flow field. The identification did not depend on the aspect ratio and geometry of the container. Steady and slow rotation of the RBC flow does not seem to have important dynamical effects for small rotation rates that correspond to $\mathrm{Ro} \gtrsim \mathcal{O}(1)$ (Niemela, Babuin, and Sreenivasan, 2010). However, experiments suggest that unsteady rotation rates (i.e., the rotation speeds are modulated) can cause major changes even at modest rotation; see Niemela, Babuin, and Sreenivasan (2010) at $\mathrm{Ra} = 10^{10}$ or Zhong, Sterl, and Li (2015) at lower Ra.

This situation changes for rapidly rotating convection. Recent investigations on the basis of reduced asymptotic models, such as the nonhydrostatic balanced equation model by Julien *et al.* (2012), and DNSs by Stellmach *et al.* (2014) and Favier, Silvers, and Proctor (2014) of the Boussinesq equations (35)–(37) demonstrate the spontaneous formation of large-scale vortices that are also identified as a condensate in Fourier space (Rubio *et al.*, 2014), with this the result of an inverse cascade, similar to two-dimensional box turbulence (Smith and Yakhot, 1993). Scaling laws for the turbulent heat transport in rapidly rotating RBC were discussed by King, Stellmach, and Aurnou (2012) and Cheng *et al.* (2015). Although the Sun does not rotate rapidly enough to reach the geostrophic regime, computational studies in solar convection at larger rotation rates such as those by Miesch, Brun, and Toomre (2006) and Miesch *et al.* (2012) indicate that similar effects are prominent at large scales, leaving smaller convection scales unaffected. A detailed morphological classification of the turbulent convection regimes in rapidly and moderately rotating stars is found in Hindman, Featherstone, and Julien (2020).

Simple estimates and experience from laboratory studies together suggest that rotation has no effect on granular scales; the effect is weak even on the supergranular scale. This conclusion has an important bearing on how one thinks about descending cold plumes (which presumably are on the scale of granules at most supergranules). The largest effect of rotation could be strong on the scale of giant cells, but their existence is not well established, as mentioned in Sec. I. It is thus conceivable that the largest effect of rotation in the Sun is felt through differential rotation only.

It is worth stressing that the flow structure in rotating convection is tightly coupled to the Prandtl number (Rossby, 1969), and the previous statements, based on studies at moderate Prandtl numbers, may need qualification when Pr is extremely small as in the Sun. Horn and Schmid (2017) and Aurnou *et al.* (2018) showed that rotating convection at low Pr does not form columnar structures along the rotation axis, as observed at $\mathrm{Pr} > 1$ [see, e.g., experiments by Aujogue *et al.* (2018)], but oscillatory convective motions do. We refer to Cheng *et al.* (2018) for a recent summary of the parameter ranges that are accessible in laboratory experiments. The absence of columnar structures is consistent with the nature of differential rotation observed in the Sun.

G. Effect of vertical magnetic fields

Experimental RBC studies in the presence of strong vertical magnetic fields are mostly conducted in liquid metals and for simple field configurations (Cioni, Chaumat, and Sommeria, 2000; Burr and Müller, 2001; King and Aurnou, 2015; Zürner *et al.*, 2020). Since the magnetic Prandtl number in laboratory flows is also low as in the Sun, typically $\mathrm{Pm} \lesssim 10^{-5}$, the magnetic Reynolds numbers $\mathrm{Rm} = \mathrm{PmRe} \ll 1$ in these studies, with this as the quasistatic regime of magnetoconvection (Zürner *et al.*, 2016). DNSs in this regime, for Chandrasekhar numbers up to $Q = 4 \times 10^6$, $\mathrm{Ra} = 10^7$, and $\mathrm{Pr} = 0.025$, have demonstrated how the magnetic field reduces the granule size and eventually suppresses them away from sidewalls once $Q \gtrsim Q_c = \mathrm{Ra}/\pi^2$ and $\mathrm{Nu} \to 1$ (Liu, Krasnov, and Schumacher, 2018). Figure 6(c) plots $Q_\odot(r)$ as a function of the radial distance. Although several simplifications enter this estimate (and caution is thus necessary), it is seen that $Q_\odot(r)$ becomes extremely large toward the surface, thus suggesting a possible damping influence on convection of the strong poloidal magnetic flux tubes that are generated.

H. Large-scale circulations

Any number of pictures of solar convection depict it in terms of large-scale circulations across the entire depth of the CZ, so it would be useful to know if such motions exist in the Sun. Weak, periodic large-scale flows are set up in turbulent RBC, even at extremely high Ra; see Krishnamurti and Howard (1981), who conducted experiments for aspect ratios of 10 to 100, $\mathrm{Ra} \le 2 \times 10^6$, and $\mathrm{Pr} \ge 7$, and Niemela and Sreenivasan (2008) for aspect ratios 4 and up to $\mathrm{Ra} = 10^{13}$. This large-scale motion is particularly ubiquitous for aspect ratios unity and below (Niemela and Sreenivasan, 2003b). The organization of turbulent convection into large-scale patterns is also known from the DNS of RBC in domains with large aspect ratios of $\Gamma \ge 10$ (Hartlep, Tilgner, and Busse, 2003; von Hardenberg *et al.*, 2008; Stevens *et al.*, 2018; Green *et al.*, 2020; Krug, Lohse, and Stevens, 2020), which are particularly pronounced in the velocity field when the turbulent flow is averaged over a finite time window (Bailon-Cuba, Emran, and Schumacher, 2010; Emran and Schumacher, 2015). Averaging over a characteristic time window τ removes fast small-scale fluctuations and reveals patterns that are reminiscent of the weakly nonlinear regime of RBC (Busse, 1978); see Fig. 11. These patterns have been termed superstructures; they evolve slowly for times $t > \tau$ (Fonda *et al.*, 2019) and obey characteristic scales that depend on Pr (Pandey, Scheel, and Schumacher, 2018) at a fixed Rayleigh number.

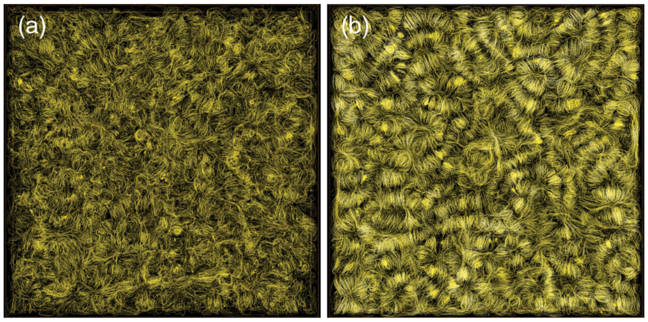

FIG. 11. Streamlines of (a) instantaneous and (b) time-averaged velocity fields viewed from the top. The averaging time in (b) is about $60H/U_f$. DNS data for $\mathrm{Ra} = 10^5$, $\mathrm{Pr} = 0.005$, and aspect ratio $\Gamma = 25$ are from Pandey, Scheel, and Schumacher (2018), who applied a spectral element method (Scheel, Emran, and Schumacher, 2013).

While the large-scale circulation is thus ubiquitous in RBC, it is notoriously unsteady for large Ra. The large-scale motions reverse directions stochastically beyond Rayleigh numbers of the order of 10^9 (Ciliberto, Cioni, and Laroche, 1996; Sreenivasan, Bershadskii, and Niemela, 2002; Brown and Ahlers, 2006; Mishra *et al.*, 2011). Glatzmaier and Roberts (1995) linked the reversal of the large-scale circulation to the erratic reversals of Earth's magnetic field. Since the reversal of magnetic field in the Sun is much more organized, a weak large-scale circulation that stochastically changes direction, even if one were to exist, is likely to be a secondary consequence of the Sun's magnetic field. In any case, the reversal rate of the large-scale flow in convection increases in frequency, so its identity and strength diminish with increasing Rayleigh number, and their very existence becomes dubious for $\mathrm{Ra} \gtrsim 10^{13}$; see Sreenivasan, Bershadskii, and Niemela (2002).

To summarize, our understanding of RBC, the paradigm for convection flows, has improved significantly in recent decades and many questions on its statistical properties, large-scale pattern formation, and turbulent transport are now answered via joint efforts that combine theoretical models, controlled laboratory experiments, and comprehensive DNS. Some of these results can guide the understanding of the more complex situation of solar convection. We attempted to draw parallels where possible but stress that analogies are at best imperfect for a full understanding.

VII. IMPLICATIONS OF A LOW THERMAL PRANDTL NUMBER

Among several lessons learned from RBC studies in Sec. VI, the one conclusion that stands out is the importance of a low Prandtl number. Massaguer and Zahn (1980) as well as Rüdiger (1989) point out that even a turbulent Prandtl number in the Sun may be small, $\mathrm{Pr}_t = \nu_e/\kappa_e \sim 0.01$ to 0.4. We thus provide some comments on this aspect.

A. Plume formation in surface convection

In Fig. 5(c) we show the temperature profile $\Theta(r)$ in the vicinity of the solar surface. The profile suggests a "thermal boundary layer" thickness δ_T of approximately 200–250 km that can be inferred, for specificity, as the intersection point of the two nearly linear slopes, corresponding to the local $\mathcal{H}_p$; see Fig. 2(e). This thermal boundary layer, which is less than 0.4% of H, may be regarded as setting the thickness of the stems of the thermal plumes that descend into the interior of the CZ. The scale is supported by closer inspection of the visible solar surface observations, for example, in Riethmüller *et al.* (2014). The strong density stratification causes a decrease of the stem width with increasing depth, a process that might compensate for turbulent dispersion and cross diffusion.

The thermal diffusivity is calculated by $\kappa_\gamma = k_\gamma/c_p\rho$. At $r \lesssim R_\odot$ this quantity passes through a minimum [see Fig. 4(b)] before becoming as large as $\kappa_\gamma \sim 10^9\ \mathrm{m}^2/\mathrm{s}$. Thus, a cross plume diffusion time $t_{\rm diff} \approx \delta_T^2/\kappa_\gamma \approx 4\times 10^{10}\,{\rm m}^2/(10^7\,{\rm m}^2\,{\rm s}^{-1}) \approx 4000\,{\rm s}$ is of the order of $\sim 10\tau_{\rm G}$ or $\tau_{\rm SG}/24$. It thus requires a downward velocity in the plume of $U_z \approx \delta_T/t_{\rm conv} \gtrsim 0.05\ {\rm km\,s}^{-1}$ to compensate for this strong molecular diffusion. In this estimate, we set $t_{\rm diff} \sim t_{\rm conv}$. This implies that a certain minimum velocity is necessary to overcome the dispersion of the plumes by molecular diffusion and to reach deeper layers in which molecular diffusion of the temperature field is significantly reduced.

There are two caveats to this conclusion. First, the turbulent thermal diffusivity will smear out the thermal plumes much faster than molecular diffusivity; here the role of the smallness of the molecular Prandtl number is that it probably influences turbulent diffusivity. As Fig. 9(g) shows in the RBC study $-\partial_z \langle T(z)\rangle_{A,t} \simeq \Delta T/H$, and thus κ_e is comparable to κ for ${\rm Pr} = 0.001$. Second, if too many plumes survive the depths of the CZ, it means that too much radial momentum is transmitted into the bulk of the CZ, thus making it harder for differential rotation to survive. It thus appears likely that only those plumes or thermals can fall down into an ever denser plasma and survive for substantial depths or even all the way to the bottom of the CZ, and they are connected with an intense vortex structure (Anders, Lecoanet, and Brown, 2019). This challenges the magnetic pumping scenario for dynamos at the tachocline.

The compressibility at the surface impacts the mean kinetic energy dissipation rate, which is given by

$$\langle\rho\epsilon\rangle = \langle\rho\epsilon_s\rangle + \langle\rho\epsilon_d\rangle = \langle\eta\boldsymbol{\omega}^2\rangle + \tfrac{4}{3}\langle\eta(\boldsymbol{\nabla}\cdot\boldsymbol{u})^2\rangle, \tag{40}$$

which is composed of solenoidal and dilatational parts with $\boldsymbol{\omega} = \boldsymbol{\nabla}\times\boldsymbol{u}$. DNSs of compressible turbulence by Sarkar *et al.* (1989) suggest a closure given by $\langle\rho\epsilon_d\rangle \simeq \langle\rho\epsilon_s\rangle M_t^2$, where $M_t = u_{\rm rms}/c_s$ is the turbulent Mach number (although the situation is likely to be more complex). Furthermore, $\langle\rho\epsilon_s\rangle \simeq \eta u_{\rm rms}^2/\lambda_T^2$, where the Taylor microscale is given by $\lambda_T \simeq \mathcal{H}_p {\rm Re}_f^{-1/2}$, giving a dissipation profile

$$\langle\rho\epsilon\rangle(r) \simeq \rho\nu\frac{\alpha^2 U_f^2}{\mathcal{H}_p^2}{\rm Re}_f(1+\alpha^2 M^2), \tag{41}$$

where $u_{\rm rms}(r) = \alpha U_f(r)$ and the Mach number $M(r) = U_f/c_s$. From Sec. VI.E, we conclude that $u_{\rm rms}(r) \simeq U_f(r)$ at low Prandtl number and from Sec. IV.B that $M \ll 1$ inside much of the CZ. Thus, one gets an estimate $\langle\rho\epsilon\rangle(r_g) \simeq \rho\nu U_f^2 {\rm Re}_f/\mathcal{H}_p^2 \approx 2000\ {\rm kg/ms}^3$ and $\langle\rho\epsilon\rangle(R_\odot) \simeq 2\rho\nu c_s^2 {\rm Re}_f/\mathcal{H}_p^2 = 10^{11}\ {\rm kg/ms}^3$. Even though these estimates have to be taken with caution, they indicate the extreme turbulence level at the surface. This enhanced mean energy dissipation rate $\langle\epsilon\rangle$ suggests a turbulent cascade between the integral scale and the Kolmogorov length. In spite of this elevated dissipation level, it is interesting that the granular structure is visibly preserved in the outer layer; see Fig. 1(a). This observation is presumably related to the fact that high turbulence levels do not yield a commensurate increase in the effective thermal diffusivity mentioned in Sec. VI.E.

B. Convection in the limit of zero Prandtl number

The importance of small Pr has already been mentioned. The main point is not that it matters everywhere in turbulence, but in deciding whether the descending thermal plumes remain stable and coherent in the stratified CZ. These are thus sufficient reasons for studying thermal convection in the limit of zero Prandtl number (Spiegel, 1962; Thual, 1992), and this was done in the Boussinesq framework. The corresponding equations in the limit ${\rm Pr} \to 0$ (which here implies taking $\kappa \to \infty$) for nonmagnetic RBC are given in dimensionless form by

$$\boldsymbol{\nabla}\cdot\boldsymbol{u} = 0, \tag{42}$$

$$\frac{D\boldsymbol{u}}{Dt} + \frac{1}{\rm Ro}(\boldsymbol{e}_z\times\boldsymbol{u}) = -\boldsymbol{\nabla}p + \frac{1}{\sqrt{\rm Gr}}\boldsymbol{\nabla}^2\boldsymbol{u} + \theta\boldsymbol{e}_z, \tag{43}$$

$$\frac{1}{\sqrt{\rm Gr}}\boldsymbol{\nabla}^2\theta = -u_z. \tag{44}$$

Temperatures are rescaled by ${\rm Pr}\,\Delta T$, and the free-fall velocity definition in Eq. (16) is consequently modified to $U_f = \sqrt{g_r {\rm Pr}\,\Delta T H/T_r}$. The equation for temperature becomes a Poisson equation. Physically, this implies that the departure from the diffusive equilibrium profile, the field $\theta(\boldsymbol{x},t) = T(\boldsymbol{x},t) - (1-z)$, is enslaved by the advecting vertical velocity component. This in turn provides a nonlinear amplification mechanism for the velocity field in the momentum balance since $\theta = -\sqrt{\rm Gr}\boldsymbol{\nabla}^{-2}u_z$ enters via the buoyancy term. The highly nonlinear driving is why the fluid turbulence in this extremely low-Prandtl-number limit becomes so highly inertial; see also Breuer *et al.* (2004) and Schumacher, Götzfried, and Scheel (2015).

For deep convection, Boussinesq equations are no longer adequate. Unfortunately, for anelastic conditions, and even less so for general convection conditions, the right equations do not yet exist. In simulations such as that of Orvedahl *et al.* (2018), whose main goal is to study the Prandtl number effects, the standard anelastic equations were used without deriving the right approximations for the limit of an extremely small Prandtl number. This remains work for the future.

VIII. POSSIBLE PLANETARY INFLUENCES

Convection, in conjunction with rotation and the magnetic field, is traditionally regarded as the sole generator of dynamics manifested on the Sun's surface (also in all of the CZ, but we focus on the surface here because we can observe it directly). Some of the magnetic events that occur on the Sun's surface, including some major storms, are consistent with the broadly stochastic nature of the convective field, but it is less clear whether the latter can also drive the nearly periodic phenomena related to sunspots: their appearance every 22 yr or so, the orderly migration of the new spots toward the equator, and their symmetry with respect to the equator (McIntosh *et al.*, 2014; Choudhuri, 2015). Rapidly rotating convection flows seem to support oscillatory large-scale dynamos (Käpylä, Mantere, and Brandenburg, 2013).

It is conceivable that such large-scale motion can develop in spherical geometry and that, in the case of the Sun, they are related to the presumed giant cells with weak amplitudes (Hathaway, Upton, and Colegrove, 2013; Bogart, Baldner, and Basu, 2015), but neither these giant cells nor any nearby subharmonics have the right regularity or temporal frequency to explain the periodicity of sunspots. Further, we have seen that the large-scale circulation in laboratory flows is erratic at higher Rayleigh numbers, becoming weak beyond a certain point. If these features carry over to the Sun, it is hard to understand how the combination of convection, rotation, and magnetic buoyancy can generate the observed recurrent nature of sunspots.

RBC develops an oscillatory component when a periodic element is superposed on the steady heating at the bottom wall, as seen in Niemela and Sreenivasan (2008). They observed that the entire convection region in the bulk of the apparatus responded to it with a similar periodic component, essentially without attenuation through the convection layer height. All attenuation occurred in the layer close to the bottom wall. Perhaps some such forcing occurs in the Sun as well. Dicke (1978) suggested a clocked process inside the Sun on the basis of available data ruling out a random walk. Abreu *et al.* (2012) discussed possible planetary influences on the Sun as the reason for this clockwork, a viewpoint that is still controversial; see, e.g., Poluianov and Usoskin (2014). It is mostly motivated by the close coincidence of the periodicity of Jupiter's orbit around the Sun with that of the sunspots. Jupiter is the most massive planet but still carries only about 0.1% of the mass of the Solar System; however, it carries about $2/3$ of the entire angular momentum of the Solar System. Detailed calculations suggest that the tidally important Jupiter-Venus-Earth system gives good agreement with sunspot characteristics. The resulting tidal height would, however, be extremely small, $h \approx 1$ mm, but corresponds by virial theorem to a velocity $v \approx \sqrt{2g(r_*)h} \sim 1$ m/s in the tachocline (Stefani, Giesecke, and Weier, 2019). This might affect the superadiabaticity and consequently the local magnetic storage capacity in the tachocline (Abreu *et al.*, 2012). It also puts further constraints on existing dynamo models; for detailed discussions see Bonanno *et al.* (2012) and Stefani *et al.* (2018).

In spite of their attractiveness, such studies are presented with a sense of apology that is prompted by the fact that there are no models that elevate quantitative agreement to the level of a dynamical connection. As already stated the tidal modifications of the Sun's surface by the planets are trivially small, as are the fluctuations caused on the magnetic and temperature fields [with the caveat that all such calculations have been made on the basis of mean values and do not allow for the fact that there could be intense fluctuations about the mean (Sreenivasan and Antonia, 1997), which causes such calculations to be unreliable]. One can presumably find local features on which such effects could be large: for example, the magnetic field at the tachocline could be influenced by the magnetic fields of Jupiter. Given that we know so little about the Sun's dynamics with certainty, our view is that one should not simply discard this possibility, even if it is not strong enough at present to provide a causal connection.

IX. SUMMARY AND CONCLUSIONS

We have discussed thermal convection in the Sun on the basis of the standard solar model S (Christensen-Dalsgaard *et al.*, 1996), and provided radial profiles of important transport coefficients with respect to radial depth. Our emphasis has also been to calculate typical dimensionless parameters, such as Rayleigh and Prandtl numbers. Any effort to understand the unusual dynamics of solar convection needs such information. We have attempted to bridge studies of the simplest case of turbulent convection, the Rayleigh-Bénard convection, in the laboratory and simulations, with convection in the Sun. The broad perspective of this Colloquium can be summarized as follows:

(i) Solar convection operates extremely close to the adiabatic thermodynamic equilibrium. Though likely to be highly turbulent, it remains close to the marginal stability boundary. This is quantified by the extremely small superadiabaticity $\Delta_s(r)$. The state variables that determine the isentropic equilibrium case vary over several orders of magnitude, with scale heights much smaller than the total height of the layer H. We recall that a RBC convection flow that is close to the marginal stability limit on several scales would obey a heat transfer scaling of $\mathrm{Nu} \sim \mathrm{Ra}^{1/3}$ following Malkus (1954). We recall also that, at least for the case with open boundaries, the scaling law has a $1/2$ power. In the absence, on the one hand, of reliable prefactors in these scaling laws, especially given the extremely low Prandtl numbers, and, on the other hand, the uncertainty associated with the proper boundary conditions, we cannot say which of the two, if either, applies to the Sun.

(ii) Convection in the outer layer is driven by the radiative cooling at the top prescribed by the luminosity flux $L_\odot$ (Nordlund, Stein, and Asplund, 2009). This allows us to estimate the dimensionless Nusselt number of the turbulent heat transfer to $\mathrm{Nu}_\odot \sim 10^6$. This cooling generates a strong negative buoyancy close to the surface, while the bulk and lower part of the convection layer remains neutrally buoyant to a good approximation. Such a regime suggests a highly asymmetric convection with strongly localized, coherent downwelling cold plumes that have to be compensated for by moderate upward flows over a larger area if one assumes that the convective motion covers the layer as a whole. O'Mara *et al.* (2016) suggested that this picture emphasizes a turbulent Prandtl number $\mathrm{Pr}_t > 1$. An open question is how such a turbulent Prandtl number can be established in a highly turbulent fluid turbulence that is driven by an extremely diffusive temperature field. Indeed, Rüdiger (1989) calculated $\mathrm{Pr}_t < 1$ in the Sun.

A study related to this surface-driven convection was made recently by Cossette and Rast (2016). Coherent thermal plumes can be expected to be subject to strong turbulent diffusion and entrainment on their decline. Vertical magnetic fields and the differential rotation can enlarge this dispersion when the flow is close to Chandrasekhar's magnetoconvection limit. We cannot be certain of any such models until we understand the relative importance of opposing phenomena but point out the analogy to conditionally unstable moist convection (Bjerknes, 1938; Pauluis and Schumacher, 2011). Here this picture of narrow cloudy air upflows and broad dry air subsidences becomes increasingly inefficient as Ra increases and thus requires additional mechanisms such as radiative cooling (Pauluis and Schumacher, 2013) that destabilize the dry air regions.

(iii) Convection in the Sun is characterized by an extremely small Prandtl number $\mathrm{Pr} \sim 10^{-6}$, dropping to even smaller values near the surface, which will forever be impossible to reproduce in the laboratory. This inhibits turbulent transport and implies that we should focus more on anelastic simplification of the equations in the limit of zero Prandtl number. (Compressibility does not seem to be a major factor except in the outermost region.) This was done in the RBC setting by Spiegel (1962). RBC studies demonstrate a highly intermittent fluid turbulence at extremely low Pr with significantly enhanced fluctuations of kinetic energy dissipation. Systematic studies of small-scale intermittency in low-Prandtl RBC, e.g., by moments of the kinetic energy dissipation rate, have started only recently (Schumacher *et al.*, 2018) and can provide further guidance for deriving SGS models beyond MLT and its refinements; see also Lohse and Xia (2010).

(iv) Solar convection is characterized by an extremely large Rayleigh number. We provided plausible estimates on the basis of pressure scale height; if the outer scale is H, which is more than 2 orders of magnitude larger than $\mathcal{H}_p$ [see Fig. 2(e)], Ra increases by 6 orders of magnitude, thus bringing us back to the estimates given in the Introduction. The characteristic velocity profile $U_f(r)$ grows steadily to extremely large velocities that are significantly larger than recent analyses of helioseismology data (Hanasoge, Duvall, and Sreenivasan, 2012). The two estimates come closer in a more recent work (Birch *et al.*, 2018), though their radial distributions distinct. Finally, we note that $U_f \ll c_s$ through the bulk of the CZ, which suggests that small-scale turbulence for scales $\ell \ll \mathcal{H}_p$ can be described and parametrized similarly to the incompressible RBC case; see also the preceding comment in (iii).

Our review of the convection in the Sun covers a large territory and the description points out, at appropriate places, the unsatisfactory state of our understanding of its dynamical features. We want to highlight three particular problems that would benefit from immediate attention. (1) Convection in highly stratified media. We think that some attention to this problem in simulations or the laboratory is much more rewarding than another study of classical RBC. (2) The analytical exploration of the fact that the temperature gradient in most of the CZ departs only by a minute amount from the adiabatic profile. It is astonishing that this marginal state of thermal transport has not been exploited successfully thus far. (3) The extremely small magnitude of thermal Prandtl number appears to endow solar convection with two special properties: high turbulence levels combined, at the same time, with an effective thermal diffusivity that approaches the molecular values from above. All three areas will benefit from more detailed studies.

Our ignorance of the dynamics of the Sun is vast, but it should not diminish the enormous strides made in the field. There are excellent reasons to think that our knowledge will become better consolidated with time, and this consolidation will come from observations of the full Sun via new space missions, helioseismic inferences, modeling and simulations (of both the Sun itself and the laboratory flows), and theory, all of which are becoming increasingly sophisticated. Further, new observations of Sun-like stars have been growing with time, and any knowledge of their dynamics (e.g., differential rotation) can shed light on the dynamics of the Sun itself. Finally, it is our belief that this effort will help us to understand other Sun-like stars and their own planetary systems, some of which could be habitable for life as we know it.

ACKNOWLEDGMENTS

We are grateful to A. Brandenburg, S. Braun, J. Christensen-Dalsgaard, C. R. Doering, L. Gizon, S. M. Hanasoge, D. Krasnov, M. S. Miesch, D. Mitra, K. Moffatt, A. Pandey, O. Pauluis, F. Stefani, S. Weiss, and T. Zürner for the discussions and comments. We thank the Tandon School of Engineering at New York University. J. S. thanks the Deutsche Forschungsgemeinschaft and K. R. S. thanks the School of Mathematics, Institute for Advanced Study, Princeton University, for its support during this work. We also acknowledge the supercomputing resources provided by Large-Scale Project No. pr62se of the Gauss Centre for Supercomputing.

REFERENCES

Abramenko, V. I., V. B. Yurchyshyn, P. R. Goode, I. N. Kitiashvili, and A. G. Kosovichev, 2012, Astrophys. J. Lett. **756**, L27.

Abreu, J. A., J. Beer, A. Ferriz-Mas, G. McCracken, and F. Steinhilber, 2012, Astron. Astrophys. **548**, A88.

Ahlers, G., S. Grossmann, and D. Lohse, 2009, Rev. Mod. Phys. **81**, 503.

Ahlers, G., X. He, D. Funfschilling, and E. Bodenschatz, 2012, New J. Phys. **14**, 103012.

Anders, E. H., D. Lecoanet, and B. P. Brown, 2019, Astrophys. J. **884**, 65.

Appourchaux, T., *et al.*, 2010, Astron. Astrophys. Rev. **18**, 197.

Asplund, M., N. Grevese, A. J. Sauval, and P. Scott, 2009, Annu. Rev. Astron. Astrophys. **47**, 481.

Augustson, K. C., A. S. Brun, and J. Toomre, 2019, Astrophys. J. **876**, 83.

Aujogue, K., A. Pothérat, B. Sreenivasan, and F. Debray, 2018, J. Fluid Mech. **843**, 355.

Aurnou, J., V. Bertin, A. M. Grannan, S. Horn, and T. Vogt, 2018, J. Fluid Mech. **846**, 846.

Babcock, H. W., 1961, Astrophys. J. **133**, 572.

Bailon-Cuba, J., M. S. Emran, and J. Schumacher, 2010, J. Fluid Mech. **655**, 152.

Balbus, S. A., J. Bonart, H. N. Latter, and N. O. Weiss, 2009, Mon. Not. R. Astron. Soc. **400**, 176.

Balbus, S. A., and J. F. Hawley, 1991, Astrophys. J. **376**, 214.

Barker, A. J., A. M. Dempsey, and Y. Lithwick, 2014, Astrophys. J. **791**, 13.

Basu, S., 2019, Physics **12**, 65.

Bates, D. R., A. E. Kingston, and R. W. P. McWhirter, 1962, Proc. R. Soc. A **267**, 297.

Bessolaz, N., and A. S. Brun, 2011, Astrophys. J. **728**, 115.

Birch, A., T. L. Duvall, Jr., L. Gizon, S. M. Hanasoge, B. Hindman, K. Nagashima, and K. R. Sreenivasan, 2018, *Proceedings of the 2018 SDO Workshop: Catalyzing Solar Connections, Ghent, Belgium*, pp. 42, https://register-as.oma.be/sdo2018/.

Bjerknes, J., 1938, Q. J. R. Meteorol. Soc. **64**, 325.

Bogart, R. S., C. S. Baldner, and S. Basu, 2015, Astrophys. J. **807**, 125.

Böhm-Vitense, E., 1954, Z. Astrophys. **34**, 209.

Böhm-Vitense, E., 1958, Z. Astrophys. **46**, 108.

Bonanno, A., A. Brandenburg, F. Del Sordo, and D. Mitra, 2012, Phys. Rev. E **86**, 016313.

Bouillaut, V., S. Lepot, S. Aumaitre, and B. Gallet, 2019, J. Fluid Mech. **861**, R5.

Brandenburg, A., 2016, Astrophys. J. **832**, 6.

Brandenburg, A., and Å. Nordlund, 2011, Rep. Prog. Phys. **74**, 046901.

Breuer, M., S. Wessling, J. Schmalzl, and U. Hansen, 2004, Phys. Rev. E **69**, 026302.

Brown, E., and G. Ahlers, 2006, J. Fluid Mech. **568**, 351.

Brummell, N., T. Cline, and F. Cattaneo, 2002, Mon. Not. R. Astron. Soc. **329**, L73.

Brun, A. S., and M. K. Browning, 2017, Living Rev. Sol. Phys. **14**, 4.

Brun, A. S., and J. Toomre, 2002, Astrophys. J. **570**, 865.

Burr, U., and U. Müller, 2001, Phys. Fluids **13**, 3247.

Busse, F. H., 1978, Rep. Prog. Phys. **41**, 1929.

Busse, F. H., and R. M. Clever, 1981, J. Fluid Mech. **102**, 75.

Caligari, P., F. Moreno-Insertis, and M. Schüssler, 1995, Astrophys. J. **441**, 886.

Calkins, M. A., J. M. Aurnou, J. D. Eldredge, and K. Julien, 2012, Earth Planet. Sci. Lett. **359–360**, 55.

Canuto, V. M., and I. Mazzitelli, 1991, Astrophys. J. **370**, 295.

Castaing, B., G. Gunaratne, F. Heslot, L. Kadanoff, A. Libchaber, S. Thomae, X.-Z. Wu, S. Zaleski, and G. Zanetti, 1989, J. Fluid Mech. **204**, 1.

Chan, K. L., and S. Sofia, 1987, Science **235**, 465.

Chandrasekhar, S., 1960, *Radiative Transfer* (Dover Publishing, Mineola, NY).

Charbonneau, P., 2010, Living Rev. Sol. Phys. **7**, 3.

Chavanne, X., F. Chillà, B. Castaing, B. Hébral, B. Chabaud, and J. Chaussy, 1997, Phys. Rev. Lett. **79**, 3648.

Cheng, J. S., J. M. Aurnou, K. Julien, and R. P. J. Kunnen, 2018, Geophys. Astrophys. Fluid Dyn. **112**, 277.

Cheng, J. S., S. Stellmach, A. Ribeiro, A. Grannan, E. M. King, and J. M. Aurnou, 2015, Geophys. J. Int. **201**, 1.

Chillà, F., and J. Schumacher, 2012, Eur. Phys. J. E **35**, 58.

Cholemari, M. R., and J. H. Arakeri, 2009, J. Fluid Mech. **621**, 69.

Choudhuri, A. R., 2015, *Nature's Third Cycle* (Oxford University Press, Oxford).

Choudhuri, A. R., and B. B. Karak, 2009, Res. Astron. Astrophys. **9**, 953.

Christensen-Dalsgaard, J., 2002, Rev. Mod. Phys. **74**, 1073.

Christensen-Dalsgaard, J., D. O. Gough, and E. Knudstrup, 2018, Mon. Not. R. Astron. Soc. **477**, 3845.

Christensen-Dalsgaard, J., *et al.*, 1996, Science **272**, 1286.

Ciliberto, S., S. Cioni, and C. Laroche, 1996, Phys. Rev. E **54**, R5901.

Cioni, S., S. Chaumat, and J. Sommeria, 2000, Phys. Rev. E **62**, R4520.

Cioni, S., S. Horanyi, L. Krebs, and U. Müller, 1997, Phys. Rev. E **56**, R3753.

Clune, T. C., J. R. Elliot, M. S. Miesch, J. Toomre, and G. A. Glatzmaier, 1999, Parallel Comput. **25**, 361.

Cossette, J.-F., and M. P. Rast, 2016, Astrophys. J. Lett. **829**, L17.

Couston, L.-A., D. Lecoanet, B. Favier, and M. Le Bars, 2017, Phys. Rev. Fluids **2**, 094804.

Cowley, C. R., 1990, Astrophys. J. **348**, 328.

Cunnyngham, I., M. Emilio, J. Kuhn, I. Scholl, and R. Bush, 2017, Phys. Rev. Lett. **118**, 051102.

Deardorff, J. W., 1966, J. Atmos. Sci. **23**, 503.

Dicke, R. H., 1978, Nature (London) **276**, 676.

Dikpati, M., and P. A. Gilman, 2007, New J. Phys. **9**, 297.

Doering, C. R., S. Toppaladoddi, and J. S. Wettlaufer, 2019, Phys. Rev. Lett. **123**, 259401.

Ecke, R. E., and J. J. Niemela, 2014, Phys. Rev. Lett. **113**, 114301.

Emran, M. S., and J. Schumacher, 2015, J. Fluid Mech. **776**, 96.

Favier, R., L. J. Silvers, and M. R. E. Proctor, 2014, Phys. Fluids **26**, 096605.

Featherstone, N. A., and B. W. Hindman, 2016, Astrophys. J. Lett. **830**, L15.

Fonda, E., A. Pandey, J. Schumacher, and K. R. Sreenivasan, 2019, Proc. Natl. Acad. Sci. U.S.A. **116**, 8667.

Freytag, B., M. Steffen, H.-G. Ludwig, S. Wedemeyer-Böhm, W. Schaffenberger, and O. Steiner, 2012, J. Comput. Phys. **231**, 919.

Fussen, D., and C. Kubach, 1986, J. Phys. B **19**, L31.

Gibert, M., H. Pabiou, F. Chillá, and B. Castaing, 2006, Phys. Rev. Lett. **96**, 084501.

Gizon, L., T. L. Duvall, Jr., and J. Schou, 2003, Nature (London) **421**, 43.

Glatzmaier, G. A., and P. H. Roberts, 1995, Nature (London) **377**, 203.

Glazier, J. A., T. Segawa, A. Naert, and M. Sano, 1999, Nature (London) **398**, 307.

Goldstein, R. J., H. D. Chiang, and D. L. See, 1990, J. Fluid Mech. **213**, 111.

Gough, D. O., and M. E. McIntyre, 1998, Nature (London) **394**, 755.

Green, G., D. G. Vlaykov, J. P. Mellado, and M. Wilczek, 2020, J. Fluid Mech. **887**, A21.

Greer, B. J., B. W. Hindman, N. A. Featherstone, and J. Toomre, 2015, Astrophys. J. **803**, L17.

Greer, B. J., B. W. Hindman, and J. Toomre, 2016, Astrophys. J. **824**, 4.

Grossmann, S., and D. Lohse, 2000, J. Fluid Mech. **407**, 27.

Grossmann, S., and D. Lohse, 2011, Phys. Fluids **23**, 045108.

Gudiksen, B. V., M. Carlsson, V. H. Hansteen, W. Hayek, J. Leenaarts, and J. Martinez-Sykora, 2011, Astron. Astrophys. **531**, A154.

Guerrero, G., P. K. Smolarkiewicz, E. M. de Gouveia dal Pino, A. G. Kosovichev, and N. N. Mansour, 2016, Astrophys. J. **819**, 104.

Hanasoge, S. M., T. L. Duvall, Jr., and K. R. Sreenivasan, 2012, Proc. Natl. Acad. Sci. U.S.A. **109**, 11928.

Hanasoge, S. M., L. Gizon, and K. R. Sreenivasan, 2016, Annu. Rev. Fluid Mech. **48**, 191.

Hanasoge, S. M., H. Hotta, and K. R. Sreenivasan, 2020, Sci. Adv. **6**, eaba9639.

Hartlep, T., A. Tilgner, and F. H. Busse, 2003, Phys. Rev. Lett. **91**, 064501.

Hathaway, D. H., J. G. Beck, R. S. Bogart, K. T. Bachmann, G. Khatri, J. M. Petitto, S. Han, and J. Raymond, 2000, Sol. Phys. **193**, 299.

Hathaway, D. H., T. Teil, A. A. Norton, and I. Kitiashvili, 2015, Astrophys. J. **811**, 105.

Hathaway, D. H., L. Upton, and O. Colegrove, 2013, Science **342**, 1217.

He, X., D. Funfschilling, H. Nobach, E. Bodenschatz, and G. Ahlers, 2012, Phys. Rev. Lett. **108**, 024502.

Hindman, B. W., N. A. Featherstone, and K. Julien, 2020, Astrophys. J. **898**, 120.

Horanyi, S., L. Krebs, and U. Müller, 1999, Int. J. Heat Mass Transfer **42**, 3983.

Horn, S., and P. J. Schmid, 2017, J. Fluid Mech. **831**, 182.

Horn, S., and O. Shishkina, 2015, J. Fluid Mech. **762**, 232.

Hotta, H., 2017, Astrophys. J. **843**, 52.

Hotta, H., H. Iijima, and K. Kusano, 2019, Sci. Adv. **5**, eaau2307.

Hotta, H., M. Rempel, and T. Yokoyama, 2015, Astrophys. J. **803**, 42.

Hotta, H., M. Rempel, and T. Yokoyama, 2016, Science **351**, 1427.

Iglesias, C. A., and F. J. Rogers, 1996, Astrophys. J. **464**, 943.

Iyer, K. P., J. D. Scheel, J. Schumacher, and K. R. Sreenivasan, 2020, Proc. Natl. Acad. Sci. U.S.A. **117**, 7594.

Jacoutot, L., A. G. Kosovichev, A. A. Wray, and N. N. Mansour, 2008, Astrophys. J. Lett. **684**, L51.

Johnston, H., and C. R. Doering, 2009, Phys. Rev. Lett. **102**, 064501.

Julien, K., A. M. Rubio, I. Grooms, and E. Knobloch, 2012, Geophys. Astrophys. Fluid Dyn. **106**, 392.

Kadanoff, L. P., 2001, Phys. Today **54**, No. 8, 34.

Kagan, D., and J. C. Wheeler, 2014, Astrophys. J. **787**, 21.

Käpylä, P. J., M. J. Korpi, A. Brandenburg, D. Mitra, and R. Tavakol, 2010, Astron. Nachr. **331**, 73.

Käpylä, P. J., M. J. Mantere, and A. Brandenburg, 2013, Geophys. Astrophys. Fluid Dyn. **107**, 244.

Käpylä, P. J., M. Rheinhardt, R. Arlt, A. Brandenburg, P. J. Käpylä, A. Lagg, N. Olspert, and J. Warnecke, 2017, Astrophys. J. Lett. **845**, L23.

Karak, B. B., J. Jiang, M. S. Miesch, P. Charbonneau, and A. R. Choudhuri, 2014, Space Sci. Rev. **186**, 561.

Khalilov, R., I. Kolesnichenko, A. Pavlinov, A. Mamykin, A. Shestakov, and P. Frick, 2018, Phys. Rev. Fluids **3**, 043503.

King, E. M., and J. M. Aurnou, 2015, Proc. Natl. Acad. Sci. U.S.A. **112**, 990.

King, E. M., S. Stellmach, and J. M. Aurnou, 2012, J. Fluid Mech. **691**, 568.

Kippenhahn, R., A. Weigert, and A. Weiss, 2012, *Stellar Structure and Evolution* (Springer, Heidelberg).

Kitiashvili, I. N., S. Couvidat, and A. Lagg, 2015, Astrophys. J. **808**, 59.

Kitiashvili, I. N., A. G. Kosovichev, N. N. Mansour, S. K. Lele, and A. A. Wray, 2012, Phys. Scr. **86**, 018403.

Kitiashvili, I. N., A. G. Kosovichev, N. N. Mansour, and A. A. Wray, 2011, Astrophys. J. **727**, L50.

Kitiashvili, I. N., A. G. Kosovichev, N. N. Mansour, and A. A. Wray, 2015, Astrophys. J. **809**, 84.

Kitiashvili, I. N., A. G. Kosovichev, N. N. Mansour, and A. A. Wray, 2016, Astrophys. J. Lett. **821**, L17.

Kraichnan, R. H., 1962, Phys. Fluids **5**, 1374.

Krasnov, D., O. Zikanov, and T. Boeck, 2011, Comput. Fluids **50**, 46.

Krishnamurti, R., and L. N. Howard, 1981, Proc. Natl. Acad. Sci. U.S.A. **78**, 1981.

Krug, D., D. Lohse, and R. J. A. M. Stevens, 2020, J. Fluid Mech. **887**, A2.

Kunnen, R. P. J., R. J. A. M. Stevens, J. Overkamp, C. Sun, G. F. van Heijst, Kupka, and H. J. H. Clercx, 2011, J. Fluid Mech. **688**, 422.

Kupka, F., and H. J. Muthsam, 2017, Living Rev. Comput. Astrophys. **3**, 1.

Landau, L. D., and E. M. Lifshitz, 1987, *Course of Theoretical Physics, Vol. 6: Fluid Mechanics* (Butterworth-Heinemann, Oxford).

Langfellner, J., L. Gizon, and A. Birch, 2015a, Astron. Astrophys. **581**, A67.

Langfellner, J., L. Gizon, and A. Birch, 2015b, Astron. Astrophys. **579**, L7.

Lantz, S. R., and Y. Fan, 1999, Astrophys. J. Suppl. Ser. **121**, 247.

Ledoux, P., M. Schwarzschild, and E. A. Spiegel, 1961, Astrophys. J. **133**, 184.

Leighton, R. B., 1964, Astrophys. J. **140**, 1547.

Lepot, S., S. Aumaitre, and B. Gallet, 2018, Proc. Natl. Acad. Sci. U.S.A. **115**, 8937.

Liu, W., D. Krasnov, and J. Schumacher, 2018, J. Fluid Mech. **849**, R2.

Lohse, D., and K.-Q. Xia, 2010, Annu. Rev. Fluid Mech. **42**, 335.

Löptien, B., L. Gizon, A. C. Birch, J. Schou, B. Proxauf, T. L. Duvall, Jr., R. S. Bogart, and U. R. Christensen, 2018, Nat. Astron. **2**, 568.

Magic, Z., R. Collet, M. Asplund, R. Trampedach, W. Hayek, A. Chiavassa, R. F. Stein, and Å. Nordlund, 2013, Astron. Astrophys. **557**, A26.

Malkus, W. V. R., 1954, Proc. R. Soc. A **225**, 196.

Massaguer, J. M., and J.-P. Zahn, 1980, Astron. Astrophys. **87**, 315.

McIntosh, S. W., *et al.*, 2014, Astrophys. J. **792**, 12.

Miesch, M. S., 2005, Living Rev. Sol. Phys. **2**, 1.

Miesch, M. S., A. S. Brun, M. L. DeRosa, and J. Toomre, 2008, Astrophys. J. **673**, 557.

Miesch, M. S., A. S. Brun, and J. Toomre, 2006, Astrophys. J. **641**, 618.

Miesch, M. S., N. A. Featherstone, M. Rempel, and R. Trampedach, 2012, Astrophys. J. **757**, 128.

Miesch, M. S., and J. Toomre, 2009, Annu. Rev. Fluid Mech. **41**, 317.

Mishra, P. K., A. K. De, M. K. Verma, and V. Eswaran, 2011, J. Fluid Mech. **668**, 480.

Mishra, P. K., and M. K. Verma, 2010, Phys. Rev. E **81**, 056316.

Mitra, D., A. Brandenburg, N. Kleeorin, and I. Rogachevskii, 2014, Mon. Not. R. Astron. Soc. **445**, 761.

Moffat, K., and E. Dormy, 2019, *Self-Exiting Fluid Dynamos* (Cambridge University Press, Cambridge, England).

Nagashima, K., A. C. Birch, J. Schou, B. W. Hindman, and L. Gizon, 2020, Astron. Astrophys. **633**, A109.

Nagayama, T., *et al.*, 2019, Phys. Rev. Lett. **122**, 235001.

Nelson, N. J., B. P. Brown, A. S. Brun, M. S. Miesch, and J. Toomre, 2014, Sol. Phys. **289**, 441.

Niemela, J. J., S. Babuin, and K. R. Sreenivasan, 2010, J. Fluid Mech. **649**, 509.

Niemela, J. J., L. Skrbek, K. R. Sreenivasan, and R. J. Donnelly, 2000, Nature (London) **404**, 837.

Niemela, J. J., and K. R. Sreenivasan, 2003a, J. Fluid Mech. **481**, 355.

Niemela, J. J., and K. R. Sreenivasan, 2003b, Europhys. Lett. **62**, 829.

Niemela, J. J., and K. R. Sreenivasan, 2006, J. Fluid Mech. **557**, 411.

Niemela, J. J., and K. R. Sreenivasan, 2008, Phys. Rev. Lett. **100**, 184502.

Nordlund, Å., R. F. Stein, and M. Asplund, 2009, Living Rev. Sol. Phys. **6**, 2.

O'Mara, B. M., M. S. Miesch, N. A. Featherstone, and K. C. Augustson, 2016, Adv. Space Res. **58**, 1475.

Oresta, P., G. Stringano, and R. Verzicco, 2007, Eur. J. Mech. B **26**, 1.

Orvedahl, R. J., M. A. Calkins, N. A. Featherstone, and B. W. Hindman, 2018, Astrophys. J. **856**, 13.

Ossendrijver, M., 2003, Astron. Astrophys. Rev. **11**, 287.

Pandey, A., J. D. Scheel, and J. Schumacher, 2018, Nat. Commun. **9**, 2118.

Parker, E. N., 1955, Astrophys. J. **122**, 293.

Parker, E. N., 1993, Astrophys. J. **408**, 707.

Passos, D., P. Charbonneau, and M. S. Miesch, 2015, Astrophys. J. Lett. **800**, L18.

Pauluis, O., and J. Schumacher, 2011, Proc. Natl. Acad. Sci. U.S.A. **108**, 12623.

Pauluis, O., and J. Schumacher, 2013, J. Atmos. Sci. **70**, 1187.

Petschel, K., S. Stellmach, M. Wilczek, J. Lülff, and U. Hansen, 2013, Phys. Rev. Lett. **110**, 114502.

Plumley, M., and K. Julien, 2019, Earth Space Sci. **6**, 1580.

Poluianov, S., and I. Usoskin, 2014, Sol. Phys. **289**, 2333.

Prandtl, L., 1925, Z. Angew. Math. Mech. **5**, 136.

Prusa, J. M., P. K. Smolarkiewicz, and A. A. Wyszogrodski, 2008, Comput. Fluids **37**, 1193.

Reif, F., 2009, *Fundamentals of Statistical and Thermal Physics* (Waveland Press, Long Grove, IL).

Rempel, M., 2012, Astrophys. J. **750**, 62.

Riethmüller, T. L., S. Solanki, S. V. Berdyugina, M. Schüssler, V. Martinez Pillet, A. Feller, A. Gandorfer, and J. Hirzberger, 2014, Astron. Astrophys. **568**, A13.

Rincon, F., 2019, J. Plasma Phys. **85**, 205850401.

Rincon, F., F. Lignièeres, and M. Rieutord, 2005, Astron. Astrophys. **430**, L57.

Rincon, F., and M. Rieutord, 2018, Living Rev. Sol. Phys. **15**, 6.

Rogers, F. J., and C. A. Iglesias, 1992, Astrophys. J. **401**, 361.

Rossby, H. T., 1969, J. Fluid Mech. **36**, 309.

Roudier, Th., J. M. Malherbe, M. Rieutord, and Z. Frank, 2016, Astron. Astrophys. **590**, A121.

Rubio, A. M., K. Julien, E. Knobloch, and J. B. Weiss, 2014, Phys. Rev. Lett. **112**, 144501.

Rüdiger, G., 1989, *Differential Rotation and Stellar Convection* (Akademie Verlag, Berlin).

Rüdiger, G., and L. L. Kitchatinov, 1996, Astrophys. J. **466**, 1078.

Sarkar, S., G. Erlebacher, M. Y. Hussaini, and H. O. Kreiss, 1989, NASA Contractor Report No. 181959, p. 31.

Scheel, J. D., M. S. Emran, and J. Schumacher, 2013, New J. Phys. **15**, 113063.

Scheel, J. D., and J. Schumacher, 2017, Phys. Rev. Fluids **2**, 123501.

Schekochihin, A. A., A. B. Iskakov, S. C. Cowley, J. C. McWilliams, M. R. E. Proctor, and T. A. Yousef, 2007, New J. Phys. **9**, 300.

Schumacher, J., V. Bandaru, A. Pandey, and J. D. Scheel, 2016, Phys. Rev. Fluids **1**, 084402.

Schumacher, J., P. Götzfried, and J. D. Scheel, 2015, Proc. Natl. Acad. Sci. U.S.A. **112**, 9530.

Schumacher, J., A. Pandey, V. Yakhot, and K. R. Sreenivasan, 2018, Phys. Rev. E **98**, 033120.

Schwarzschild, K., 1906, Nachr. Ges. Wiss. Goettingen Math.-Phys. Kl. **1906**, 41.

Shcheritsa, O. V., A. V. Getling, and O. S. Mazhorova, 2018, Phys. Lett. A **382**, 639.

Shi, N., M. S. Emran, and J. Schumacher, 2012, J. Fluid Mech. **706**, 5.

Siggia, E. D., 1994, Annu. Rev. Fluid Mech. **26**, 137.

Singh, N. K., I. Rogachevskii, and A. Brandenburg, 2017, Astrophys. J. Lett. **850**, L8.

Smith, L. M., and V. Yakhot, 1993, Phys. Rev. Lett. **71**, 352.

Solanki, S. K., B. Inhester, and M. Schüssler, 2006, Rep. Prog. Phys. **69**, 563.

Spiegel, E. A., 1962, J. Geophys. Res. **67**, 3063.

Spiegel, E. A., 1963, Astrophys. J. **138**, 216.

Spiegel, E. A., and J.-P. Zahn, 1992, Astron. Astrophys. **265**, 106.

Spitzer, L., 1962, *Physics of Fully Ionized Gases* (Interscience Publishers, New York).

Spruit, H. C., 1974, Sol. Phys. **34**, 277.

Spruit, H. C., Å. Nordlund, and A. M. Title, 1990, Annu. Rev. Astron. Astrophys. **28**, 263.

Sreenivasan, K. R., and R. A. Antonia, 1997, Annu. Rev. Fluid Mech. **29**, 435.

Sreenivasan, K. R., A. Bershadskii, and J. J. Niemela, 2002, Phys. Rev. E **65**, 056306.

Steenbeck, M., F. Krause, and K.-H. Rädler, 1966, Z. Naturforsch. **21A**, 369.

Stefani, F., A. Giesecke, N. Weber, and T. Weier, 2018, Sol. Phys. **293**, 12.

Stefani, F., A. Giesecke, and T. Weier, 2019, Sol. Phys. **294**, 60.

Stellmach, S., M. Lischper, K. Julien, G. Vasil, J. S. Cheng, A. Ribeiro, E. M. King, and J. M. Aurnou, 2014, Phys. Rev. Lett. **113**, 254501.

Stevens, R. J. A. M, H. J. H. Clercx, and D. Lohse, 2010, New J. Phys. **12**, 075005.

Stevens, R. J. A. M, D. Lohse, and R. Verzicco, 2011, J. Fluid Mech. **688**, 31.

Stevens, R. J. A. M., A. Blass, X. Zhu, R. Verzicco, and D. Lohse, 2018, Phys. Rev. Fluids **3**, 041501(R).

Strugarek, A., P. Beaudoin, P. Charbonneau, and A. S. Brun, 2018, Astrophys. J. **863**, 35.

Thual, O., 1992, J. Fluid Mech. **240**, 229.

Tobias, S. M., N. H. Brummell, T. L. Clune, and J. Toomre, 1998, Astrophys. J. Lett. **502**, L177.

Toppaladoddi, S., S. Succi, and J. S. Wettlaufer, 2017, Phys. Rev. Lett. **118**, 074503.

Toppaladoddi, S., and J. S. Wettlaufer, 2018, Phys. Rev. Fluids **3**, 043501.

Török, T., and B. Kliem, 2005, Astrophys. J. Lett. **630**, L97.

Tritton, D. J., 1988, *Physical Fluid Dynamics* (Oxford University Press, Oxford).

Urban, P., P. Hanzelka, T. Králík, M. Macek, V. Musilová, and L. Skrbek, 2019, Phys. Rev. E **99**, 011101.

Urban, P., P. Hanzelka, V. Musilová, T. Králík, M. La Mantia, A. Srnka, and L. Skrbek, 2014, New J. Phys. **16**, 053042.

van Ballegooijen, A. A., 1982, Astron. Astrophys. **113**, 99.

Verma, M. K., 2018, *Physics of Buoyant Flows: From Instabilities to Turbulence* (World Scientific, Singapore).

Verzicco, R., and K. R. Sreenivasan, 2008, J. Fluid Mech. **595**, 203.

Vigeesh, G., J. Jackiewicz, and O. Steiner, 2017, Astrophys. J. **835**, 148.

Vitense, E., 1953, Z. Astrophys. **32**, 135.

Viviani, M., J. Warnecke, M. J. Käpylä, P. J. Käpylä, N. Olspert, E. M. Cole-Kodikara, J. J. Lehtinen, and A. Brandenburg, 2018, Astron. Astrophys. **616**, A160.

Vögler, A., S. Shelyag, M. Schüssler, F. Cattaneo, T. Emonet, and T. Linde, 2005, Astron. Astrophys. **429**, 335.

von Hardenberg, J, A. Parodi, G. Passoni, A. Provenzale, and E. A. Spiegel, 2008, Phys. Lett. A **372**, 2223.

Weiss, N. O., and M. R. E. Proctor, 2014, *Magnetoconvection* (Cambridge University Press, Cambridge, England).

Weiss, S., R. J. A. M. Stevens, J.-Q. Zhong, H. J. H. Clercx, D. Lohse, and G. Ahlers, 2010, Phys. Rev. Lett. **105**, 224501.

Weiss, S., P. Wei, and G. Ahlers, 2016, Phys. Rev. E **93**, 043102.

Woodward, M. F., 2016, Mon. Not. R. Astron. Soc. **460**, 3292.

Wray, A. A., K. Bensassi, I. N. Kitiashvilli, N. N. Mansour, and A. G. Kosovichev, 2015, arXiv:1507.07999.

Zhong, J.-Q., S. Sterl, and H.-M. Li, 2015, J. Fluid Mech. **778**, R4.

Zhu, X., V. Mathai, R. J. A. M. Stevens, R. Verzicco, and D. Lohse, 2018, Phys. Rev. Lett. **120**, 144502.

Zhu, X., V. Mathai, R. J. A. M. Stevens, R. Verzicco, and D. Lohse, 2019, Phys. Rev. Lett. **123**, 259402.

Zhu, X., R. J. A. M. Stevens, O. Shishkina, R. Verzicco, and D. Lohse, 2019, J. Fluid Mech. **869**, R4.

Zürner, T., W. Liu, D. Krasnov, and J. Schumacher, 2016, Phys. Rev. E **94**, 043108.

Zürner, T., F. Schindler, T. Vogt, S. Eckert, and J. Schumacher, 2020, J. Fluid Mech. **894**, A21.

Zwaan, C., 1978, Sol. Phys. **60**, 213.

See Supplemental Material at http://link.aps.org/supplemental/10.1103/RevModPhys.92.041001 for a list of important constants, the derivation of transport coefficients, the anelastic and Boussinesq approximations, and an overview of numerical models of solar convection.